Journal of Volcanology and Geothermal Research 441 (2023) 107876

Contents lists available at ScienceDirect

Journal of Volcanology and Geothermal Research

journal homepage: www.journals.elsevier.com/journal-of-volcanology-and-geothermal-research

The post-2016 long-lasting Vulcanian activity of Sabancaya volcano (Peru) and associated aeolian remobilisation of volcanic ash

Allan Fries [a,*], Lucia Dominguez [a], Paul A. Jarvis [a,b], Marco Pistolesi [c], Nelida Manrique [d], Rigoberto Aguilar [d,e], David Valdivia [d], Eduardo Rossi [a], Stefano Pollastri [a], Claire J. Horwell [f], Costanza Bonadonna [a]

[a] Département des Sciences de la Terre, Université de Genève, rue des Maraîchers 13, 1205 Genève, Switzerland
[b] GNS Science, Lower Hutt, New Zealand
[c] Dipartimento di Scienze della Terra, Università degli Studi di Pisa, Via Santa Maria 53, 56126 Pisa, Italy
[d] Instituto Geológico Minero y Metalúrgico-INGEMMET, Observatorio Vulcanológico del INGEMMET, Barrio Magisterial Nro. 2 B-16 Umacollo, 04013 Yanahuara, Arequipa, Peru
[e] Laboratoire Magmas et Volcans, Université Clermont Auvergne, CNRS, IRD, OPGC, 63000 Clermont-Ferrand, France
[f] Institute of Hazard, Risk and Resilience, Department of Earth Sciences, Durham University, Durham, United Kingdom

ARTICLE INFO

Keywords:
Sabancaya volcano
Vulcanian eruptions
Tephra deposits
Volcanic ash
Aeolian remobilisation
Particle morphology

ABSTRACT

The characterisation of tephra deposits resulting from almost simultaneous sedimentation and wind remobilisation is complex, and multidisciplinary strategies are required in order to accurately constrain associated processes and eruptive parameters. We present a multifaceted study that aims to characterise the recent eruptive activity and the subsequent aeolian remobilisation of tephra deposits at Sabancaya volcano (Peru), which started erupting in November 2016 with frequent and relatively small explosions (plume heights <6 km above the vent). First, we estimated the bulk volume of tephra deposit produced between November 2016 and August 2018 at 0.04 ± 0.02 km^3, and the dense rock equivalent (DRE) volume at 0.02 ± 0.01 km^3. This corresponds to a tephra production rate of $1.1 \pm 0.5 \times 10^{-3}$ km^3 DRE per month. Second, continuous sampling in a dedicated tephra collector network between April 2018 and November 2019 allowed estimation of the tephra volume at $2.3 \pm 1.1 \times 10^{-5}$ km^3 DRE per month, indicating a significant decrease in the mass eruption rate since 2018. Third, by characterising the pulsatory activity through the repose interval between explosions and magma characteristics, Sabancaya's activity was classified as Vulcanian. Finally, aeolian remobilisation phenomena were studied using high-resolution videos, measurements of the airborne concentration of particulate matter with a diameter of $\leq$10 μm (PM_{10}) and particle physical characterisation. Subtle morphological differences are identified between remobilised particles and those in primary deposits, and we found that particles moving at ground level and above 1.5 m have grainsizes transportable by saltation and suspension, respectively.

1. Introduction

Volcanic eruptions are associated with a variety of hazards that can potentially persist over long periods of time (Siebert et al., 2010; Barclay et al., 2019). Furthermore, many volcanoes are known to experience eruptive stages during which frequent pulsatory explosions represent long-lasting hazards to the exposed communities, over weeks to decades. Recent notable examples include Soufrière Hills, Montserrat (Druitt et al., 2002); Arenal, Costa Rica (Cole et al., 2005); Colima, Mexico (Varley et al., 2010); Tungurahua, Ecuador (Eychenne et al., 2013); Fuego, Guatemala (Naismith et al., 2019) and Sakurajima, Japan (Poulidis et al., 2019). These volcanoes are characterised by sequences of explosive events of similar intensity, separated by time intervals varying from a few seconds to several days that constitute pulsatory activity, which are typical of Strombolian (Taddeucci et al., 2015) and Vulcanian (Clarke et al., 2015) eruptions.

Sabancaya volcano (Peru) has also been characterised by pulsatory activity since 2016. The area around the volcano is sparsely populated but, nonetheless, Sabancaya poses a threat to the communities inhabiting the Colca River valley (about 30,000 inhabitants). The nearest

* Corresponding author.
E-mail address: allan.fries@unige.ch (A. Fries).

https://doi.org/10.1016/j.jvolgeores.2023.107876
Received 3 March 2023; Received in revised form 5 July 2023; Accepted 23 July 2023
Available online 25 July 2023

villages are 19 km north whilst grazing areas are found between 10 and 15 km from the volcano (e.g., Aguilar, 2019). Volcanic ash has also been reported to reach the city of Arequipa, the second largest city of Peru, 70 km to the southeast (Manrique et al., 2018a; Del Carpio Calienes et al., 2020). Moreover, aeolian remobilisation (i.e., wind erosion) of loose volcanic material is observed at Sabancaya, representing an additional long-lasting secondary hazard (Wilson et al., 2011; Forte et al., 2018), which can impact wider areas than primary fallout, over extended periods of time (from syn-eruptive to millennia after an eruption) (Dominguez et al., 2020a). This also affects the properties of tephra deposits that are key to assessing the eruptive parameters of past eruptions (Pyle, 1989; Fierstein and Nathenson, 1992; Bonadonna et al., 2015, 2016; Houghton and Carey, 2015; Constantinescu et al., 2022).

Aeolian remobilisation processes include any sediment transport driven by the wind and is controlled by complex interactions between meteorological conditions, soil surface properties, particle characteristics, topography and local roughness elements (Bagnold, 1941; Liu et al., 2014; Panebianco et al., 2017; Del Bello et al., 2018; Etyemezian et al., 2019; Dominguez et al., 2020b; Jarvis et al., 2020). Particles are lifted off the ground when aerodynamic forces become greater than resisting gravitational and cohesive forces (i.e., when the wind friction velocity becomes greater than the threshold friction velocity of the particles) (Appendix A; Shao and Lu, 2000). Once mobilised, the type and duration of transport depend on the particle settling and wind friction velocities (Appendix A; Scott et al., 1995; Kok et al., 2012; Mingari et al., 2020). For typical aeolian conditions on Earth, particles with diameters ranging from 70 to 500 μm will frequently undergo saltation, with coarser particles moving by creep and those finer becoming suspended in the short (≤days) or long term (weeks-months) (Pye, 1987).

Both primary volcanic activity and secondary aeolian remobilisation occur simultaneously at Sabancaya, which therefore constitutes a suitable natural laboratory for the study of syn-eruptive remobilisation. In this particular context, the emission of fresh tephra is continuously replenishing the sediment supply over time, and the distinction between primary and remobilised particles is a challenge (Jarvis et al., 2020). Although previous studies mainly described specific remobilisation events (e.g., Folch et al., 2014), or tephra deposits of short-lived eruptions (compared to the timescales of aeolian processes) affected by wind-remobilisation (e.g., Dominguez et al., 2020b), the effect of syn-eruptive aeolian remobilisation on tephra deposits remains poorly understood. Aeolian remobilisation of volcanic ash also represents an on-going hazard (Wilson et al., 2011; Forte et al., 2018); consequently recent work has investigated the applicability of volcanic ash dispersal models for simulating such events (Folch et al., 2014; Hammond and Beckett, 2019; Mingari et al., 2020). However, knowledge of the physical properties and processes of ash remobilisation sources, from field (Dominguez et al., 2020b) and experimental work (Etyemezian et al., 2019; Del Bello et al., 2018, 2021), is necessary to improve forecast models and ultimately better understand the hazard posed by aeolian remobilisation (Liu et al., 2014; Jarvis et al., 2020; Mingari et al., 2020). Among the key parameters to assess, it is particularly important to quantify the grain-size distribution of particles remobilised by aeolian processes (Jarvis et al., 2020), notably by studying deposited particles (Wilson et al., 2011; Liu et al., 2014) using sediment traps (Arnalds et al., 2013; Panebianco et al., 2017; Dominguez et al., 2020a), airborne particle counters (Elissondo et al., 2016), and through the development of additional sampling strategies.

We have conducted a multidisciplinary study for the characterisation of both tephra sedimentation and syn-eruptive aeolian remobilisation at Sabancaya volcano. First, we examined the primary tephra deposit using both stratigraphic sections and a network of dedicated ash collectors installed in February 2018. Second, we characterised the pulsatory explosive activity of Sabancaya by analysing the variation in the repose intervals between explosions and the magma viscosity, as derived from geophysical data and geochemical models, respectively. Third, we report observations of aeolian remobilisation events and categorise them, notably based on their timing and intensity. Finally, we analysed remobilised ash particles collected using an innovative sampling method and compared their properties (i.e., size and morphology) with those from samples of primary material.

2. Explosive activity at Sabancaya and geographic setting

Sabancaya (5970 m above sea level; a.s.l.) in southern Peru is located in the Central Volcanic Zone (CVZ) of the Andes, 70 km northwest of Arequipa (Fig. 1A). The current activity at Sabancaya started in 2012 with an increase in gas emissions and seismicity (Jay et al., 2015; Machacca et al., 2023) before the onset of magmatic activity in November 2016 (Manrique et al., 2018a; Del Carpio Calienes et al., 2020; MacQueen et al., 2020). Since then, Sabancaya has shown a pulsatory explosive activity up to the time of writing (March 2023) which is characterised by several Vulcanian explosions per day. In general, the heights of the plumes have progressively decreased since the start of the eruption (Coppola et al., 2022), with plumes up to 5500 m above the vent in July 2017 (Manrique et al., 2018a) and to 4000 m above the vent in 2020 (Machacca et al., 2021).

The seismicity and geodesy of the volcano are actively monitored by the Instituto Geofísico del Perú (IGP) through its Centro Vulcanológico Nacional (CENVUL) and the Observatorio Vulcanológico del INGEMMET (OVI) based on real-time data streaming and surveys that include visual observations (Aguilar et al., 2021; Machacca et al., 2021, 2023; Coppola et al., 2022). Monitoring also comprises a dedicated tephra collector network distributed around the volcano in order to collect the primary tephra fallout from which the accumulated mass load and the thickness can be determined over extended periods of time (several months). The whole-rock geochemistry of tephra samples (including ballistic clasts) collected in 2017 indicate homogeneous andesitic compositions, with a silica content representing 59.8–62.8% of the mass (Manrique et al., 2018b).

Coppola et al. (2022) identified 6 phases of activity from November 2016 to December 2020. First, a short vent-clearing phase marked the beginning of the eruption with frequent explosions (Phase I: November – December 2016). This phase was followed by the growth of a first lava dome accompanied by intense, but fluctuating, explosive activity (Phase II: December 2016 – January 2018). The number of explosions decreased, and the growth of the lava dome stopped, during a phase of general stability (Phase III: January 2018 – March 2019). Following this period, both the growth of the dome and the explosive activity increased again (Phase IV: March – October 2019). The next phase was characterised by the lowest number of explosions associated with the collapse of the lava dome and the crater (Phase V: November 2019 – September 2020). Finally, Coppola et al. (2022) reported the formation of a second lava dome that started to grow in September 2020, accompanied by the renewal of the explosive activity (Phase VI: September – December 2020). Based on the height of the ash plumes, Coppola et al. (2022) estimated the mass of tephra erupted by Vulcanian explosions. Hence, for the whole eruptive period between November 2016 and December 2020, Coppola et al. (2022) calculated a dense rock equivalent (DRE) volume of tephra of 0.004–0.009 km^3, using magma and deposit densities of 2700 and 1000 kg m^{-3}, respectively. Satellite observations of the crater and lava domes for the same period were used to estimate a volume of about 0.002 km^3 DRE erupted during effusive phases (Coppola et al., 2022).

Before the present activity of the volcano, a similar cycle of Vulcanian and phreatomagmatic explosions of andesitic to dacitic composition took place at Sabancaya between 1990 and 1998 (Thouret et al., 1994; Juvigné et al., 1998, 2008; Gerbe and Thouret, 2004; Samaniego et al., 2016), after a period of unrest that started in December 1986. During this eruptive cycle, the mean production rate of magma has been estimated to be low, at 0.001–0.01 km^3 per year, with a peak phase from May to October 1990 that produced about 0.025 km^3 of tephra at the beginning of the eruption (Thouret et al., 1994; Gerbe and Thouret,

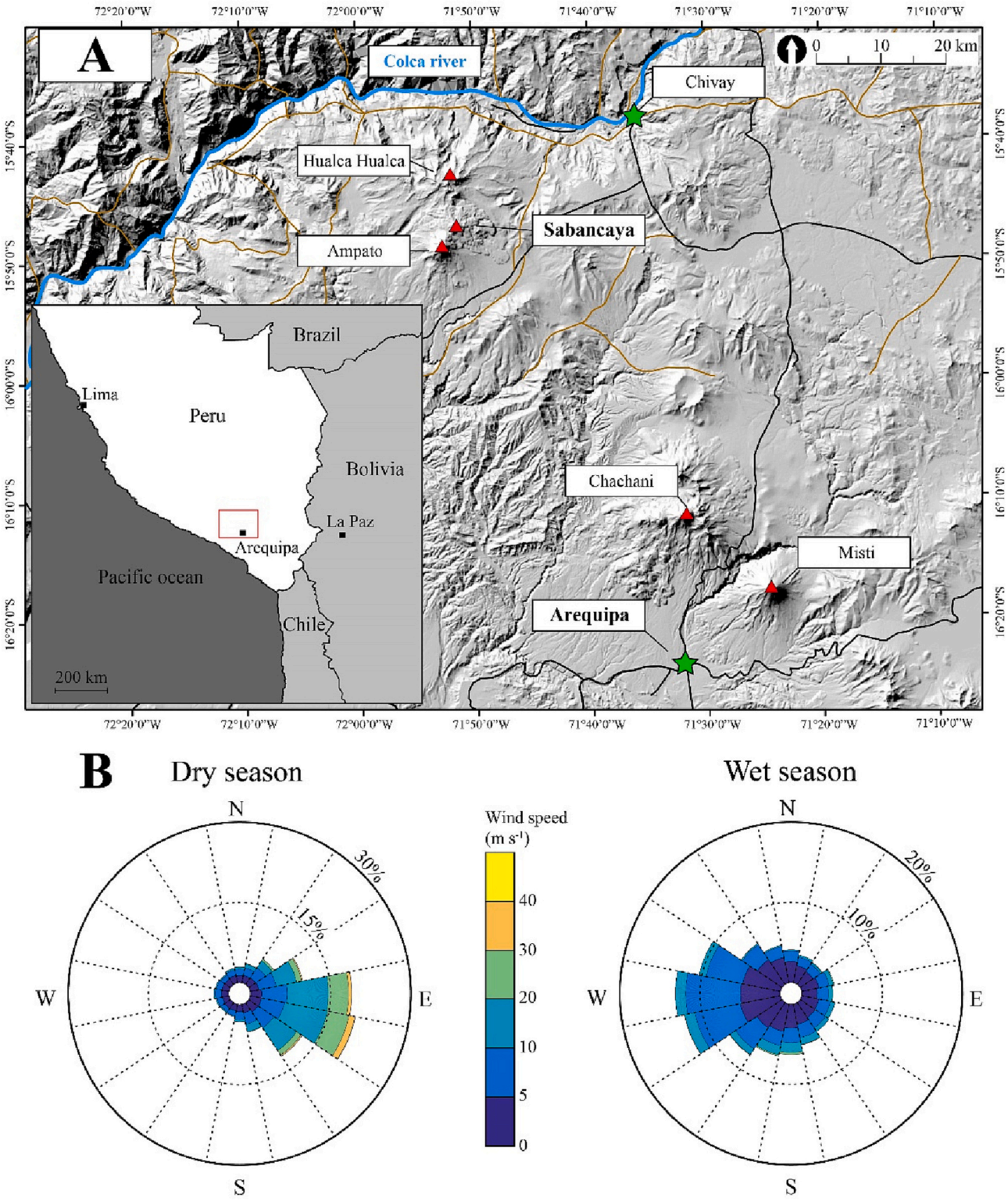

Fig. 1. A. Location of Sabancaya volcano. The region presented here corresponds to the red area in the inset regional map. Green stars and red triangles indicate cities and volcanic edifices, respectively. The blue, black and brown lines represent the Colca river and main and secondary roads, respectively. B. Wind roses (i.e., the relative frequency of wind directions and speeds) at Sabancaya from November 2016 (start of the eruption) to November 2021. The wind roses are displayed separately for the dry (May to October) and the rainy (November to April) seasons. Wind directions are averaged between 6 and 11 km a.s.l.; i.e., from the height of the vent up to the maximum height of the volcanic plumes. Wind data are from the ECMWF (European Centre for Medium-range Weather Forecasts) ERA5 reanalysis dataset (Hersbach et al., 2020) and obtained using the Matlab package TephraProb, developed by Biass et al. (2016).

2004). The plume heights significantly decreased, changing from plumes 3–7 km above vent level (a.v.l) in 1990–1992 to plumes <1 km a.v.l. after 1997 (Gerbe and Thouret, 2004). Simultaneously, the componentry of the ejecta substantially changed with time. In 1990, juvenile fragments constituted only 10–15% of the ejecta. This proportion increased to 40–50% of the material emitted in 1992–1997, with a slight decrease in 1995–1997. Juvenile fragments were eventually absent after 1997 (Gerbe and Thouret, 2004).

Few historical eruptions have been attributed to Sabancaya prior to the 1990–1998 eruptive cycle, with mentions in Spanish chronicles of only two events during the 18th century (Thouret et al., 1994), confirmed by the presence of a 10–30 cm coarse ash layer dated at 265 ± 30 BP (Samaniego et al., 2016). Additionally, the study of peat sections near Sabancaya by Juvigné et al. (2008) reveals the presence of four phreatomagmatic tephra units dated at 1870–2120 BP, 2170–2440 BP, 4120–4520 BP and 9440 to 9770 BP and tentatively attributed to eruptions originating from the local volcanoes (Ampato and/or Sabancaya). They also discovered the presence of Plinian tephra fall layers that can be related to the large regional tephra fallout from the 1600 CE eruption of Huaynaputina, for which the Volcanic Explosivity Index

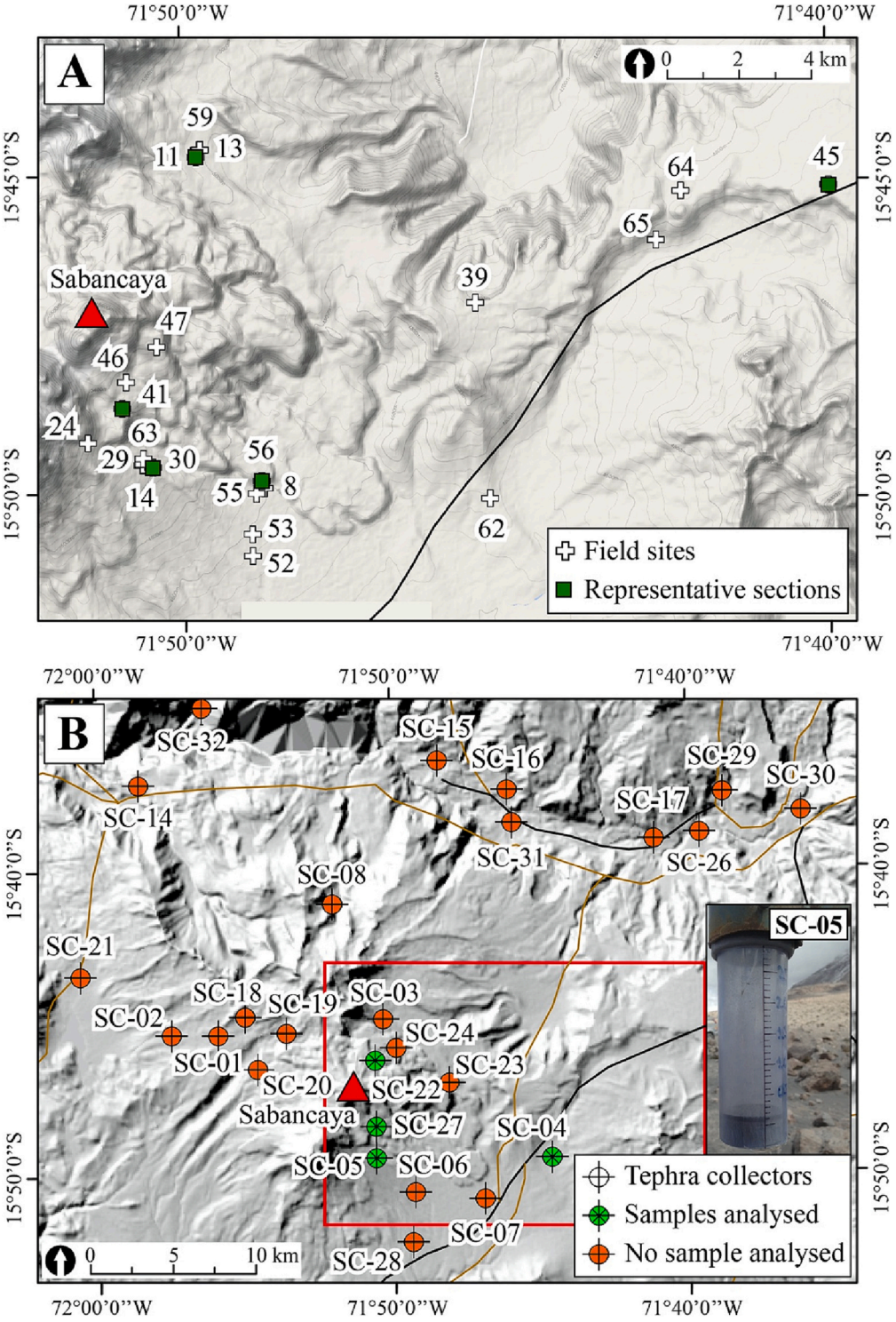

Fig. 2. A. Location of stratigraphic sections. Numbers correspond to the field sites. The green rectangles indicate the location of the reference stratigraphic sections. B. Location of the OVI tephra collectors represented by the crossed circles. The red rectangle indicates the area represented in panel A. Inset in the bottom right shows the tephra collector SC-05 on the flanks of Ampato on 2 August 2018. Green circles with a double cross highlight the location of tephra collectors for which samples have been analysed to obtain associated grainsize distributions.

(VEI) has been estimated at 6 (Adams et al., 2001; Thouret et al., 2002; Prival et al., 2020), and to the 2030 BP eruption of Misti (Cobeñas et al., 2012). The analysis of Juvigné et al. (2008) suggests that the explosive activity at Sabancaya was sporadic before the 1990–1998 eruptive cycle, with long repose periods in between eruptions. This is confirmed by the study of Samaniego et al. (2016) which identified at least 6 eruptions in the last 4000–5000 years, including the historical 1990–1998 and 18th century events. Whilst the activity was mainly effusive 6000 to 3000 years ago during the formation of Sabancaya edifice, it became mostly explosive 3000 years ago. In general, the eruptive rate is estimated at 5–7 $\times$ 10^{-4} km^3 per year at Sabancaya in the last 3000 years (Samaniego et al., 2016).

The altiplano, on which Sabancaya sits, is an arid area, with scarce vegetation that is limited to shrubs and short grasses (<1 m). Total annual precipitation is meagre, below 100 mm per year, with a dry and cold season from May to October and a wet and warm season from November to April (Supplementary Fig. S1). Wind directions up to 5 km above the vent also exhibit a marked seasonality, with a prevailing direction towards the east during the dry season and towards the west during the rainy season (Thouret et al., 1994; Fig. 1B). The meteorological conditions and the poor vegetation cover of the terrain around Sabancaya are favourable to the remobilisation of loose volcanic ash that stays exposed to the wind for long durations (Jarvis et al., 2020).

3. Methods

3.1. Field measurements and sampling (tephra deposits, tephra collectors and tephra fallout)

A field campaign was conducted at Sabancaya from 27 July to 12 August 2018 in order to study proximal to medial primary tephra deposits (<25 km from the source; Fig. 2A), tephra sedimentation and aeolian remobilisation processes. In addition to stratigraphic analyses, various sampling strategies were applied for collecting primary tephra fallout and remobilised volcanic particles separately. During this field campaign, plumes up to 3 km a.v.l. were observed (Simionato et al., 2022). The detailed list of field sites and collected samples can be found in Supplementary Table S1.

During the field campaign, 21 stratigraphic sections were studied in the northern, southern and eastern parts of the volcanic edifice, at distances between about 2 and 21 km from the vent (Fig. 2A; Table S1). Due to the difficult access in the western part of the edifice, and due to the presence of blocky lava flows of about 300–400 m high on the eastern and north-eastern flanks of Sabancaya (Bulmer et al., 1999; Samaniego et al., 2016), a detailed study of these areas around the volcano was not possible. The field investigation mainly took place south of the edifice, in glacial valleys that are associated with gentle slopes (Alcalá-Reygosa et al., 2011). At least 5 tephra units were identified and measured throughout these stratigraphic sections. This study is focused on the top layers associated with the ongoing eruption of Sabancaya and the subsequent aeolian remobilisation of these deposits. Samples were processed for grainsize, particle shape and density analysis. Since topographic surface characteristics can influence the preservation of tephra deposits (Dugmore et al., 2018), field sites were selected on the basis of two main criteria. First, stratigraphic sections were studied in flat areas, where post-deposition slope processes were unlikely to have affected the primary deposits (Selby, 1982). Second, the presence of local roughness elements (e.g., vegetation and rocks) that can affect the preservation of the deposits in their vicinity (Kok et al., 2012; Cutler et al., 2018; Dominguez et al., 2020b) was also noticed.

The OVI monitoring network includes 33 tephra collectors that have been installed within a 35 km radius around Sabancaya (Fig. 2B) in order to measure the evolution of the cumulative mass of primary tephra fallout since February 2018 (Valdivia, 2019). Collectors consist of robust vertical funnel-shaped containers, upward-facing openings, inspired by the design described in Bernard (2013). They can be used to study tephra accumulations up to 30 mm in thickness. Due to the challenging field conditions and the remoteness of their emplacement sites, collectors are unevenly distributed, and tephra collection is performed by the INGEMMET staff during missions about two to three times a year. Because of difficult accessibility, there is a lack of collectors southwest of the vent (Fig. 2B). The morphology and grainsize of 17 tephra samples derived from tephra collectors (samples labelled 'sab'; Fig. 3A; Table 1; Supplementary Table S1) have been quantified. The location of the collectors from which samples have been analysed is highlighted in Fig. 2B.

In order to integrate the cumulative sampling of tephra collectors, real-time sampling of primary tephra fallouts was performed on adhesive paper during fieldwork (samples labelled 'prim.'; Fig. 3A), similarly to the setup of Bonadonna et al. (2011). Airborne particles stick on the adhesive paper, which was mounted onto a thin section for subsequent grainsize and shape analysis with a reflected light microscope. In total, 12 primary samples were collected on the flanks of Ampato (4 km south of the vent) (Fig. 3B) during two successive explosions on 2 August 2018.

3.2. Observations and real-time sampling of aeolian remobilisation

Airborne particles associated with aeolian remobilisation events were also collected on vertical and horizontal adhesive paper at different sites (Fig. 3B). These remobilised particles were sampled at two different heights and orientation: (i) >1.5 m above the ground (samples labelled R150; Fig. 3A), with the thin section held vertically and facing the upwind direction, and (ii) by placing the adhesive paper face up at ground level (samples labelled R0; Fig. 3A). During field experiments, sampling of remobilised particles was complemented by that of the most surficial ground layer upwind of the thin section location (samples labelled 'SG'; Fig. 3A). This sample is characteristic of the source material from which airborne remobilised particles originate.

In order to measure the concentration of fine ash in suspension (diameter $d \leq 10$ μm) and to complement the sampling of remobilised volcanic ash on adhesive paper, in-situ measurements of particulate matter with a diameter ≤10 μm (PM_{10}) were conducted around the volcanic edifice. PM_{10} measurements were performed using a portable aerosol monitor that operates with a light-scattering laser photometer (TSI SidePak AM520 PM_{10}) with a recording frequency of 1 s. PM_{10} concentrations were recorded for durations of 1 to 5 h at five locations (Fig. 3C; Table 2).

Finally, High Definition (HD; 1920 × 1080 px) and High Speed (HS; 3200 frames s^{-1}) videos of remobilisation events were acquired with a Canon Legria HFG40 and a Phantom Miro M110 HS Camera mounted with a 60 mm Nikon lens, respectively. HD videos were used to image, describe and classify aeolian remobilisation events according to the categories of lithometeors proposed by Dominguez et al. (2020b), whilst HS videos were used to investigate remobilisation mechanisms at the scale of the particles (38.5 μm px^{-1}). To do so, the HS camera was placed on the ground and triggered for a duration of 1 s when particles were seen in motion.

3.3. Particle characterisation: size, morphology, density and composition

The particles collected during the field campaign were characterised using specific analytical strategies, depending on the type of sample. In particular, distinct methods were used to analyse loose samples and the particles collected on adhesive paper (Fig. 3A). A summary of the analytical strategy is provided in Supplementary Table S2.

Tephra samples obtained from collectors and from stratigraphic sections, as well as SG samples, were dried for 24 h in an oven at 80 °C before obtaining their grainsize distributions (GSD) by manual sieving down to 0 ϕ (i.e., 1 mm; $\phi = -log_2 d$, with d the particle diameter in mm; Inman, 1952). The grainsize distribution of the fraction finer than 0 ϕ ($d < 1$ mm) was measured by a combination of laser diffraction and

Table 1
Ash collector samples analysed with the BetterSizer S3 Plus to obtain the grainsize distribution and the morphology of primary ash fallouts.

Sample	Collector	Sampling dates	Sampling duration (days)	Latitude	Longitude	Distance from the vent (km)
sab-1726	SC-27	23 Jun. to 25 Jul. 2017	33	−15.647165	−71.660010	2.7
sab-1832	SC-27	07 Apr. to 25 May 2018	49	−15.647165	−71.660010	2.7
sab-1847	SC-22	22 May to 23 Jun. 2018	32	−15.764047	−71.831625	3.7
sab-1850	SC-27	27 May to 20 Jun. 2018	24	−15.647165	−71.660010	2.7
sab-1852	SC-04	25 May to 20 Jun. 2018	26	−15.824344	−71.744081	12.8
sab-1854	SC-05	25 May to 19 Jun. 2018	25	−15.824365	−71.843434	4.4
sab-1869	SC-05	19 Jun. to 28 Jul. 2018	39	−15.824365	−71.843434	4.4
sab-1890	SC-05	28 Jul. to 06 Dec. 2018	131	−15.824365	−71.843434	4.4
sab-1892	SC-27	20 Jun. to 06 Dec. 2018	169	−15.806825	−71.842863	2.7
sab-1895	SC-22	23 Jun. to 07 Dec. 2018	167	−15.764047	−71.831625	3.7
sab-1926	SC-27	15 Apr. to 20 Aug. 2019	127	−15.806825	−71.842863	2.7
sab-1927	SC-05	06 Apr. to 20 Aug. 2019	136	−15.824365	−71.843434	4.4
sab-1947	SC-04	21 Aug. to 22 Oct. 2019	62	−15.824344	−71.744081	12.8
sab-1948	SC-05	21 Aug. to 22 Oct. 2019	62	−15.824344	−71.744081	4.4
sab-1957	SC-22	15 May to 24 Oct. 2019	160	−15.764047	−71.831625	3.7
sab-1963	SC-27	20 Aug. to 28 Nov. 2019	100	−15.806825	−71.842863	2.7
sab-1967	SC-04	15 Oct. to 28 Nov. 2019	44	−15.641568	−71.765053	12.8

dynamic image analysis using a BetterSizer S3 Plus analyser. The final GSD of each sample was then calculated from merging the grainsize distributions above and below 0 ϕ to obtain the weight percentage of each size class i as follows

$$m_i^{wt\%} = \frac{m_i^{BS\ wt\%} m_{>0\phi}}{m_t} + m_i^{sieving}, \quad (1)$$

where $m_i^{BS\ wt\%}$ is the weight percentage obtained with the BetterSizer S3 Plus, $m_{>0\phi}$ is the mass of the fraction finer than 0 ϕ ($d < 1$ mm), m_t is the total mass of the sample, and $m_i^{sieving}$ is the weight percentage of class i obtained by sieving. Based on the final GSD, the median diameter Md_Φ and the sorting coefficient of Inman (1952) $\sigma_\Phi = (\sigma_{84\Phi} - \sigma_{16\Phi})/2$ were calculated, with $\sigma_{16\Phi}$ and $\sigma_{84\Phi}$ being the 16th and 84th percentiles of the grainsize distribution in Φ units, respectively.

The morphology of particles finer than 0 ϕ ($d < 1$ mm) was obtained from images acquired with the BetterSizer S3 Plus. During measurements, particles are dispersed in water and pumped through a sample cell where they are imaged by two CCD (Charge-Couple Device) cameras operating at different magnifications. Only the low magnification camera, which was best adapted to the GSDs of our samples, was used to capture images of the particles at a resolution of 14.4 μm px^{-1}. Individual particle images were first filtered automatically and manually in order to remove touching and out-of-focus particles. The remaining images were then binarized and analysed in order to obtain the equivalent particle diameter $d_{eq} = 2\sqrt{A_p/\pi}$, with A_p the area of a particle, as well as their form factor, solidity and convexity, which are important shape parameters for measuring the morphological and textural roughness of particles (Liu et al., 2015; Dürig et al., 2018; Dominguez et al., 2020b; Ross et al., 2022).

The form factor describes the general roundness of the particles, with values of 1 indicative of spherical particles. It is defined as a ratio of the area to the squared perimeter of a particle (form factor $= 4\pi A_p/P_p^2$, with P_p the perimeter of a particle). Solidity corresponds to the ratio of the particle area to the area of its bounding convex hull (solidity $= A_p/A_{ch}$, with A_{ch} the area of the bounding convex hull) and provides a measure of the morphological roughness of the particles. The convexity, meanwhile, is defined as the ratio of the perimeters of the convex hull and the particle (convexity $= P_{ch}/P_p$, with P_{ch} the perimeter of the convex hull), and yields information on the textural morphology (i.e., the roughness of the particle surface). For both convexity and solidity, values close to 1 indicate that the particles are smooth and rounded.

Shape parameters were calculated for particles with pixel densities greater or equal to 250 px per particle, which correspond to particles with $d_{eq} \geq 250$ μm, as calculated using the expression for d_{eq} above. This threshold value is lower than the minimum critical pixel density of 750 px per particle suggested by Liu et al. (2015) for estimating the solidity, and much lower than the typical recommendation of 5000 px per particle (Dellino and La Volpe, 1996; Mele et al., 2011; Schmith et al., 2017). In fact, robust shape parameter assessments require high pixel densities, especially for perimeter-dependent parameters, e.g., the form factor and the convexity, which are particularly sensitive to details of the particle outline. Particles with pixel densities less than the recommended 750 px per particle were nonetheless analysed to enable the measurements of particles between 250 and 500 μm which constituted a significant proportion of our samples, whilst particles with $d_{eq} \geq 500$ μm were captured with resolutions >750 px per particles.

Samples of airborne particles collected on adhesive paper were analysed with a reflected light microscope (Olympus BX61) equipped with an automated stage for Multi Image Alignment (MIA). MIA allowed capturing the entire surface of the adhesive paper in a single operation at a resolution of 2.2 μm px^{-1}. Images were then treated manually in order to contour the particles before binarization, which was facilitated by the high contrast between the light-coloured primary ash particles and the black tape (see Supplementary Fig. S2). The binary images were analysed in ImageJ to obtain d_{eq} for particles with pixel densities >15 px per particles (i.e., $d_{eq} \geq 10$ μm). This lower limit for particle size measurements was set to distinguish between particles and artifacts in binary images. Additionally, an ImageJ macro based on the work of Liu et al. (2015) was used to calculate shape descriptors for particles with pixel densities greater or equal to 250 px per particle. Morphological analyses were therefore limited to particles with $d_{eq} \geq 40$ μm. Although the threshold for the minimum pixel density is low, this value was nonetheless selected to enable the measurements of particles with $d_{eq} \leq 63$ μm. The typical pixel density of particles below 63 μm was 250–650 px per particle, whilst particles between 63 and 125 μm were associated with pixel densities of 650–2500 px per particle and particles larger than 125 μm were imaged with densities >2500 px per particle.

Similarly to the analysis performed with the BetterSizer S3 Plus, the form factor, solidity and convexity of the airborne particles collected on adhesive paper were also obtained. Since the quantification of particle morphology relies on different methods for loose material (i.e., dynamic image analysis) and for samples collected on adhesive paper (i.e., microscope analysis), only the shape descriptors of samples analysed with the same methods were compared. Quantifying the discrepancies related to the difference in analytical methods is beyond the scope of this study.

The morphological properties of particles from R0, R150 and primary samples were compared through statistical tests conducted with the Matlab program DendroScan (Dürig et al., 2020). First, Levene tests were applied to check whether the variances of the datasets were homogeneous. Based on the results of Levene tests, pooled or separated variance t-tests were then conducted to investigate whether the mean

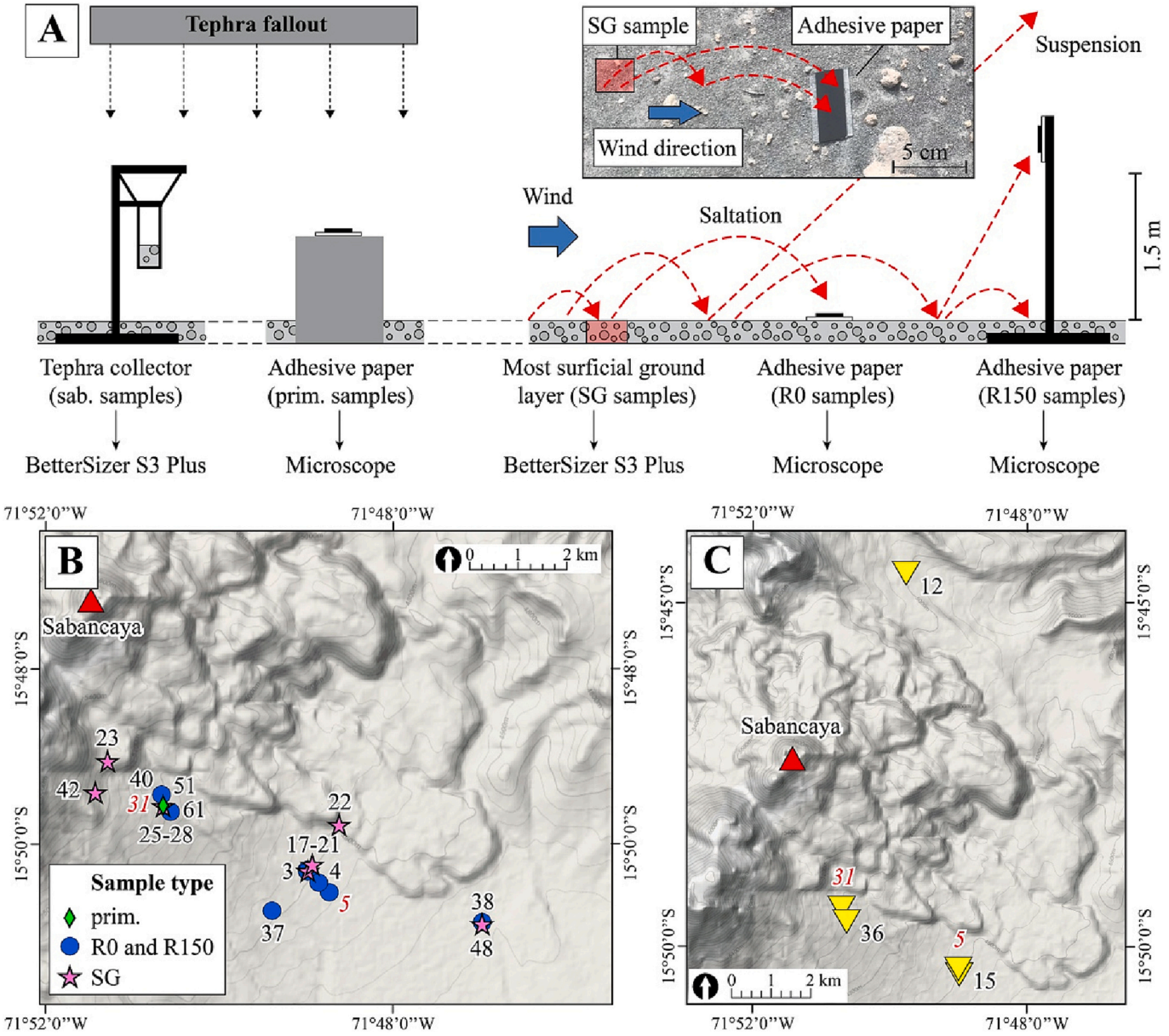

Fig. 3. A. Sampling strategies applied for the collection of primary tephra fallout and remobilised particles (see Supplementary Table S2 for additional information on the analytical procedure). Inset picture shows the collection of remobilised particles on adhesive paper at the level of the ground (R0 samples). Red arrows represent possible trajectories of remobilised particles. B. Location of the samples of airborne material collected on adhesive paper, with primary ash fallouts (prim. samples), remobilised material (R0 and R150 samples) and samples of the most surficial ground layer (SG samples) represented by green diamonds, blue circles and pink stars, respectively. C. Locations of PM_{10} (particulate matter with a diameter ≤10 μm) measurements (Table 2) represented by yellow triangles. Numbers correspond to the field sites (Supplementary Table S1). Field sites 5 and 31, where both PM_{10} measurements and sampling of remobilised material were performed, are highlighted in red and italic.

Table 2
Information on PM_{10} measurements: Date, duration (time is given in Peru standard time PET), location (also see inset map of Fig. 2B), average PM_{10} concentration (over the entire measurement duration) and description of remobilisation phenomena observed during the time of measurements (Fig. 9). When reported, drifting/blowing ash and ash whirls were observed sporadically, whilst ash storms occurred throughout the duration of measurements with varying intensity.

Site	Date	Time (hh:mm)	Duration (hh:mm)	Latitude	Longitude	Average concentration (mg m^{-3})	Remobilisation phenomena observed
5	29 Jul. 2018	12:06–14:30	02:24	−15.836799	−71.815849	0.36	Drifting/blowing ash and ash whirls
12	30 Jul. 2018	09:46–11:46	02:00	−15.744903	−71.828286	0.01	Drifting/blowing ash and ash whirls
15	31 Jul. 2018	11:35–15:46	04:11	−15.836247	−71.815980	0.01	Drifting/blowing ash and ash whirls
31	03 Aug. 2018	09:27–15:22	04:55	−15.822000	−71.843777	0.23	Ash storm
36	04 Aug. 2018	10:36–11:47	01:11	−15.825111	−71.842083	0.87	Ash storm

shape parameter values of different datasets (R0, R150, primary) showed significant differences. This was verified for p values below a significance level of 0.05, which rejected the null hypothesis that particles originated from the same population. Finally, datasets that did not show significant differences after applying a t-test were tested for statistical equivalence using equivalence tests (Dürig et al., 2021).

For microscope analysis, the total volume of the particles in a size class i was given by the sum of the equivalent volumes V_i^{eq} of all the particles with a d_{eq} belonging to size class i. The GSD of the sample was then calculated in volume percentage (vol%) by dividing the volume of particles in each size class by the total volume of the particles in the sample V_t (Freret-Lorgeril et al., 2019)

$$V_i^{vol\%} = \sum_i \frac{V_i^{eq}}{V_t}, \quad (2)$$

where $V_i^{vol\%}$ is the vol% of particles in the size class i. GSDs in vol% were later converted to wt% by assuming that the particle density did not depend on the particle size for the diameter range analysed with the microscope.

Density measurements of particle skeleton (including non-connected porosity) were performed for the size fractions finer than 0 ϕ ($d < 1$ mm). Using an Ultrapyc 1200e Helium pycnometer, three samples (sab-1869, sab-1890 and sab-1892; Table 2) from tephra collectors were analysed, as well as one sample of each stratigraphic unit, including SG samples. The density of crushed samples of primary tephra fallout was measured to enable DRE (Dense Rock Equivalent) estimates. Additionally, the density of the deposits was estimated by measuring the mass of 10 cm^3 samples contained in a graduated cylinder with a Mettler Toledo PM100 high precision balance. The uncertainty on these density measurements was constrained from the dispersion of the results obtained for 3 samples (sab-1869, sab-1890 and sab-1892).

The percentage of juvenile fragments was estimated from componentry analyses for 2 primary tephra samples (sab-1869 and sab-1895) and 3 different stratigraphic units (A – site 30, B – site 30 and C – site 13) identified during our fieldwork. For this purpose, the juvenile material with diameters smaller than 0 Φ ($d > 1$ mm) was manually separated from lithic clasts while observing them with a binocular microscope (Supplementary Fig. S3). Juvenile material consists of dark, poorly vesicular and highly porphyritic clasts (Manrique et al., 2018a, 2018b), similar to the products of the 1990–1998 eruption (Gerbe and Thouret, 2004).

The groundmass glass composition was obtained with a Jeol JXA-8200 electron microprobe at the University of Geneva, using a 15 kV accelerating voltage with an emission current of 6 nA and a probe diameter of 10 μm. The analyses were carried out on dense ballistic fragments (sab-1813) ($d \sim 60$ cm) that followed a ballistic trajectory after ejection and that were sampled at a distance of about 500 m from the vent on 06 April 2018 (Supplementary Table S1). Additionally, the groundmass glass composition of juvenile volcanic ash was analysed for 3 different stratigraphic units (A – site 30, B – site 30 and C – site 13) and 4 primary ash samples (sab-1726, sab-1832, sab-1869 and sab-1895) that were considered representative of the melt composition (Table 3).

3.4. Erupted volume and mass

Isopach maps were drawn from the thicknesses of the different units measured during our field campaign (27 July to 12 August 2018). Isopach contours were constrained only for the top tephra layers analysed at field sites corresponding to flat areas where deposits were undisturbed by surface elements. Estimation of the volume of tephra deposit was inferred using methods based on the thinning of the deposits with distance from the vent, e.g. exponential (Pyle, 1989; Fierstein and Nathenson, 1992), power-law (Bonadonna and Houghton, 2002) and Weibull (Bonadonna and Costa, 2012, 2013) fits, using the Matlab function *TephraFits* (Biass et al., 2019). Uncertainties on results given by each integration method were assessed using the stochastic method of Biass et al. (2013). To do so, 1000 runs were performed for each

Table 3
Composition (major elements) of groundmass glasses and percentage of juvenile fragments. The table presents average values, with standard deviation in brackets. [(a)]Analyses of tephra sampled during the previous eruption (1990–1998) are from Gerbe and Thouret (2004).

Sample	sab-2[(a)]	sab-9218[(a)]	sab-941a[(a)]	sab-943[(a)]	sab-9719[(a)]	sab-1726	sab-1813	sab-1832	sab-1869	sab-1895	A-30	B-30	C-13a	C-13b
Year	1990	1992	1994	1994	1997	2017	2018	2018	2018	2018	2016–2018	2016–2018	?	?
Juveniles (%)	10–15	40–50	40–50	40–50	< 40–50	–	–	–	91	94	87	77	< 25	< 25
Number of analyses	8	5	3	7	3	10	10	12	11	9	12	11	9	4
SiO_2	76.4 (1.3)	72.8 (0.8)	75.7 (0.6)	74.2 (1.8)	78.2 (0.4)	74.8 (1.2)	73.2 (0.8)	74.5 (2.6)	74.2 (2.5)	73.3 (3.6)	74.6 (1.6)	75.2 (1.2)	72.0 (2.0)	72.5 (1.4)
TiO_2	0.5 (0.1)	0.6 (0.1)	0.4 (0.3)	0.5 (0.1)	0.4 (0.05)	0.1 (0.01)	0.1 (0.01)	0.1 (0.02)	0.6 (0.2)	0.6 (0.1)	0.6 (0.1)	0.6 (0.1)	0.7 (0.3)	0.6 (0.1)
Al_2O_3	11.8 (0.8)	12.7 (0.5)	12.1 (0.5)	12.7 (0.9)	10.8 (0.2)	12.3 (0.6)	13.2 (0.2)	12.6 (1.4)	13.4 (1.4)	13.3 (2.9)	12.9 (1.0)	12.7 (1.1)	14.1 (1.2)	13.2 (1.8)
FeO	1.1 (0.2)	1.5 (0.1)	1.3 (0.2)	1.2 (0.1)	1.1 (0.1)	1.5 (0.1)	1.6 (0.1)	1.3 (0.6)	1.3 (0.3)	1.5 (0.2)	1.5 (0.2)	1.4 (0.1)	1.7 (0.8)	1.1 (0.2)
MgO	0.2 (0.1)	0.1 (0.05)	0.06 (0.02)	0.1 (0.1)	0.04 (0.01)	0.1 (0.05)	0.2 (0.01)	0.2 (0.3)	0.1 (0.1)	0.2 (0.1)	0.2 (0.1)	0.1 (0.04)	0.3 (0.2)	0.08 (0.03)
MnO	0.03 (0.03)	0.03 (0.05)	0 (0)	0.1 (0.2)	0.05 (0.01)	0.03 (0.03)	0.02 (0.02)	0.2 (0.3)	0.03 (0.02)	0.01 (0.01)	0.02 (0.02)	0.02 (0.02)	0.04 (0.01)	0.04 (0.02)
CaO	0.5 (0.2)	0.5 (0.1)	0.2 (0.1)	0.4 (0.1)	0.5 (0.1)	0.4 (0.1)	0.6 (0.03)	0.8 (0.6)	1.0 (0.8)	1.1 (1.7)	0.6 (0.2)	0.6 (0.5)	1.0 (0.5)	0.6 (0.5)
Na_2O	2.9 (0.5)	3.2 (0.3)	2.9 (0.1)	2.8 (0.7)	2.6 (0.4)	3.3 (0.3)	3.5 (0.4)	3.2 (0.6)	3.8 (0.6)	3.7 (0.6)	3.6 (0.6)	3.7 (0.3)	4.3 (0.5)	3.5 (0.6)
K_2O	5.8 (0.3)	6.1 (0.1)	6.0 (0.2)	6.2 (0.6)	5.7 (0.2)	5.6 (0.2)	5.4 (0.1)	5.3 (0.5)	5.3 (0.5)	5.3 (1.1)	5.4 (0.3)	5.5 (0.5)	5.3 (0.6)	6.1 (0.3)
Total	99.2	97.7	98.7	98.3	99.2	98.2	97.8	98.1	99.7	99.0	99.4	99.9	99.4	97.8

calculation, using randomly sampled values in the uncertainty range around each parameter. Errors of 30 and 40% were assumed for thickness measurements (Engwell et al., 2013) and data contouring (Klawonn et al., 2014a, 2014b), respectively.

Additionally, a map was compiled based on the mass load accumulated monthly in tephra collectors (kg m^{-2} $month^{-1}$), with observations spanning three overlapping periods from April 2018 to November 2019. The three periods considered are: i) from April 2018 to October 2019, for tephra collectors west of the vent; ii) from May 2018 to October 2019, for tephra collectors mainly located east of the vent; and iii) from July 2018 to November 2019, for the most proximal and distal tephra collectors. The calculation of the average mass of tephra deposited monthly was based on these three periods, as they were associated with the highest number of available measurements and the widest spatial

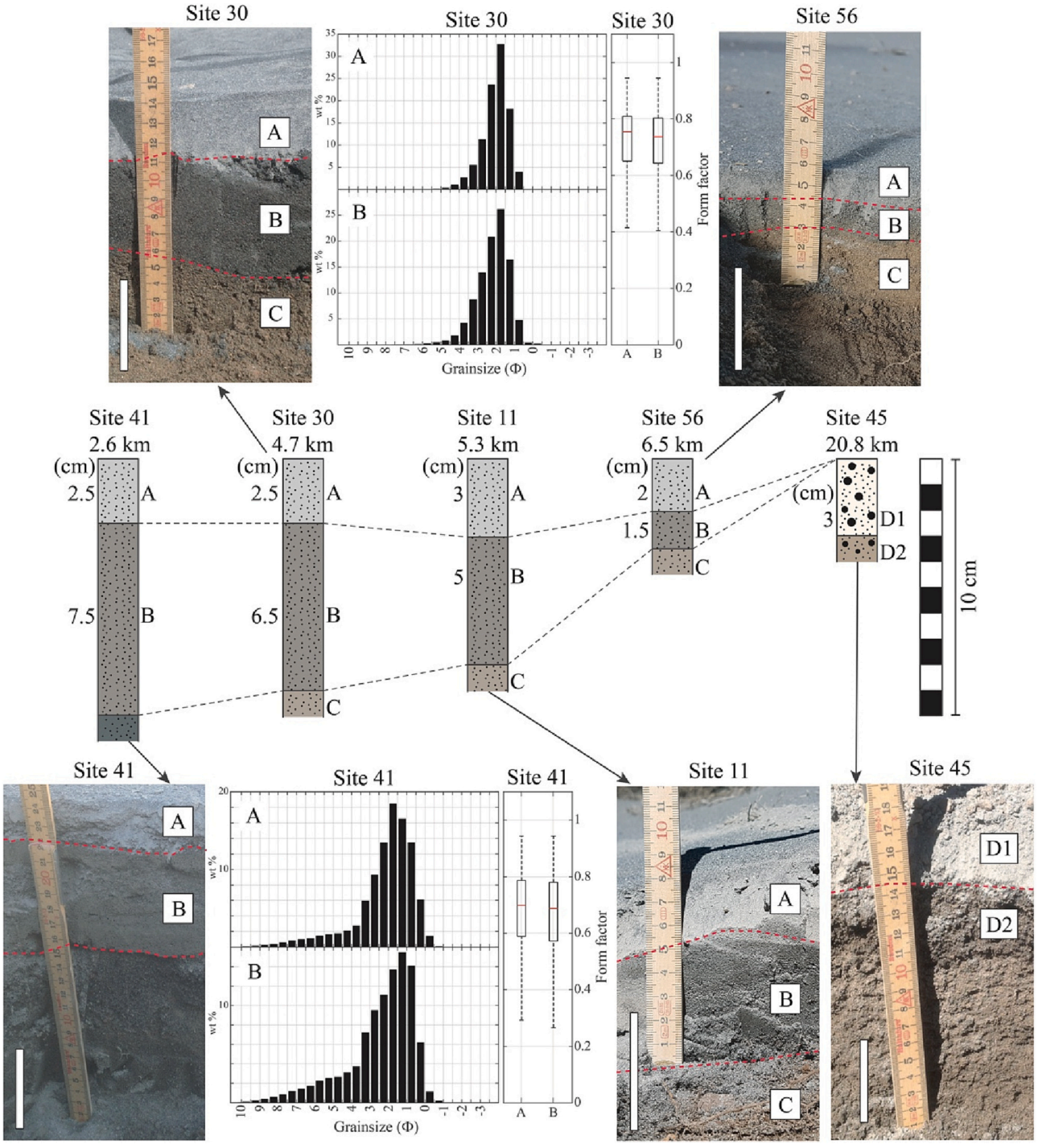

Fig. 4. Stratigraphic sections of the most surficial tephra deposits associated with Sabancaya. Tephra deposits are correlated between sections arranged from the closest to the furthest of the vent (from left to right) and correspond to the green rectangles in Fig. 1C. Distances from the vent are given above sketches of the sections. Each section is illustrated by a photograph (the white bars are 5 cm long in all images), with additional grainsize and morphology measurements shown for sites 41 and 30. The general roundness of the particles is expressed through the form factor shape parameter in box and whisker plots, with the red lines representing the median of the distribution, the lower and upper limits of the boxes indicating the 25th and 75th percentiles and the dashed lines extending to the 1st and 99th percentiles.

distribution for compiling the isomass map. Similar to the volume calculations, the mass erupted each month was estimated based on the exponential, power-law and Weibull methods and then converted to erupted volume based on the deposit density estimation.

3.5. Explosion frequency and classification

Pulsatory volcanic activity can be quantified by the intensity and frequency of explosive events. Very frequent (i.e., very short repose times of the order of 0.1 to 10 s) explosions can produce sustained lava fountains resulting in the emission of steady plumes (Valentine and Gregg, 2008; Ripepe et al., 2013; Dürig et al., 2015; Bonadonna et al., 2023) whilst less frequent (i.e., longer repose times) explosions preferentially generate transient plumes (Varley et al., 2006; Chojnicki et al., 2015). The eruptive style of Sabancaya was determined following the methodology of Dominguez et al. (2016), who showed the correlation between the distribution of the repose times and the viscosity of magmas. The frequency of explosions and the repose time intervals of consecutive single events were investigated by cross-checking seismic data recorded by the OVI seismic stations and visual observations (Machacca et al., 2021; Coppola et al., 2022) from the beginning of the explosive activity in November 2016 until May 2021. Seismic events with an energy >0.1 MJ were associated with visible explosions producing pyroclastic material, enabling filtering of the seismic signal.

For the classification of the explosions based on their frequency, the distribution of the repose time between single events was analysed by applying the log-logistic renewal process following the methodology of Dominguez et al. (2016) described in Appendix B. To this end, the magma viscosity was constrained based on the models of Giordano et al. (2008), for the melt viscosity, and Costa et al. (2009) for the bulk viscosity. The melt composition was constrained from the groundmass glass compositions of the tephra produced between June and July 2017 (sab-1726) and between April and July 2018 (sab-1813, sab-1832 and sab-1869), whilst the same water contents of 0.8–2.2 wt% and crystallinity of 25 vol% reported by Gerbe and Thouret (2004) were used, given the similarities in the magma composition between the current eruptive activity and the 1990–1998 cycle. A melt temperature of 900 °C was assumed as an average value for similar magma compositions such as for the eruptions of Santiaguito, Guatemala (Scott et al., 2012) and Ubinas, Peru (Rivera et al., 2014).

4. Results

4.1. Tephra deposits

The tephra deposits located at distances <25 km from the vent can be divided into five main layers: A, B, C, D1 and D2 (Fig. 4). While layers A, B and C are found and correlated at distance <10 km from the vent, only layers D1 and D2 can be found at more distal locations. Table 3 presents the groundmass glass composition and the percentage of juvenile fragments for layers A, B and C, as well as for primary tephra samples and tephra emitted during the 1990–1998 eruption (Gerbe and Thouret, 2004). All samples are characterised by rhyolitic groundmass glass compositions (≥ 72 wt% SiO_2) highly enriched in K_2O (>5 wt%).

Layer A represents the top of the stratigraphic sections. It is composed of uncompacted, grey, well-sorted ash (Md_Φ values between 1.5 and 2.6 Φ, and σ_Φ between 0.8 and 1.5 Φ), covered by a millimetric (<5 mm) layer of coarser, less sorted ash (Md_Φ = 1.0–2.6 Φ, σ_Φ varying from 0.8 to 3.3 Φ). The thickness of layer A varies locally, notably as a function of the surface elements (e.g., vegetation cover, presence of boulders, topography; Supplementary Table S1). For example, at 6.5 km southeast from the vent, it varies from 5 cm inside plants to 2 cm outside. Moreover, the thickness of layer A does not decrease gradually with distance from the vent but is rather uniform and generally between 2 and 3 cm in the entire studied area (Fig. 4). The local variations in thickness, the presence of ripples at the surface of the deposits (Supplementary Fig. S4) and of cross-bedding structures in layer A, along with the looseness of the material, suggest that layer A has undergone wind-driven erosion and deposition and is probably continuing to be remobilised.

Layer B is composed of compacted dark grey ash, located below layer A, and stratified in multiple sub-layers in most proximal locations (e.g., site 41; Fig. 4). Sub-layers could not be correlated between sections. The GSDs of layers A and B are very similar (Md_Φ = 1.4–3.3 Φ and σ_Φ = 0.8–2.7 Φ; Fig. 4), and their groundmass glass composition is nearly identical (e.g., 74.6 and 75.2 wt% SiO_2 for layers A and B, respectively; Table 3), with similar percentages of juvenile fragments (87% for layer A and 77% for layer B at site 30; Table 3). The form factor values of particles in layers A and B are also comparable, with 90% of the particles between 0.3 and 0.8, and median form factors of 0.7 (Fig. 4). Similar to layer A, the thickness of layer B varies at the local scale in association with the presence of surface elements (Supplementary Table S1). Conversely, the thickness of layer B also clearly varies as a function of distance from the vent along the prevailing wind direction, passing from 18 cm at 2 km E of the vent (site 47) to 1.5 cm at 6.5 km (site 56). Similarly to layer A, the local variation in the thickness of layer B, along with the presence of fine ash lenses (Dominguez et al., 2020b) suggests that layer B could have been affected by syn-eruptive remobilisation, as is the case for layer A, while the overall decay of the thickness trend suggests it is a primary layer.

Layer C is a brown, compacted tephra layer (Md_Φ = 2.6–2.8 Φ and σ_Φ = 0.9–1.5 Φ) that constitutes the base of the stratigraphic section (Fig. 4). Layer C is distinguished from layers A and B by its larger amount of lithics (juvenile fragments account for <25%; Table 3), and it appears less fresh and often representing a horizon within which small roots are located. This low percentage of juvenile fragments is similar to the previous 1990–1998 eruptive episode (Table 3; Gerbe and Thouret, 2004). The groundmass glass composition of layer C is comparable to that of the least evolved material erupted in 1992.

In more distal stratigraphic sections (at distances >10 km from the vent; e.g., site 45 in Fig. 4), only Layers D1 and D2 can be observed. D1 is an uncompacted light grey layer laying on top of D2, a compacted brown layer. These layers have different grainsize characteristics than those observed in proximal areas, with GSDs considerably coarser (Md_Φ = −1.3–0.4 Φ) and less sorted (σ_Φ = 2.5–3.0 Φ).

Given the similarities between layers A and B in terms of composition, componentry and morphology and their distribution at the top of the stratigraphic sections, they likely correspond to tephra fallouts from the current cycle (post-2016) of explosions of Sabancaya. The only difference observed between layers A and B is the level of compactness, with the loose material of layer A emplaced above the compacted layer B. In contrast, layer C can be attributed to the 1990–1998 eruption of Sabancaya. Finally, D1 and D2 cannot be correlated with proximal Layers A, B or C; they were not related to specific recent eruptions at Sabancaya and may represent older eruptive cycles or deposits which were affected by intense post-eruptive remobilisation.

4.2. Tephra sampled in vertical collectors and adhesive paper

The GSDs of the primary tephra sampled in the tephra collectors are unimodal and relatively fine, with a median particle diameter finer than 1 Φ (500 μm) (Fig. 5A). As expected for low-intensity explosions, such as those produced by Sabancaya, the mode of these GSDs rapidly decreases with distance from the source, passing from 1.5 to 1 Φ (355–500 μm) at 2.7 km from the vent to 2.5–2 Φ (180–250 μm) at 12.8 km from the vent. Accordingly, Md_Φ changes from 1.5 to 2.1 Φ (350 to 230 μm) and σ_Φ changes from 1.0 to 0.8 Φ (500 to 580 μm). The results of morphometric analysis for individual samples can be found in Supplementary Data S1. Values of the solidity of primary tephra are principally between 0.8 and 1.0, with 90% of the particles in that range. The convexity is mostly between 0.9 and 1 for 90% of the particles (Fig. 5A). The DRE density is 2802.2 ± 11.3 kg m^{-3}, while the bulk density of the material sampled in

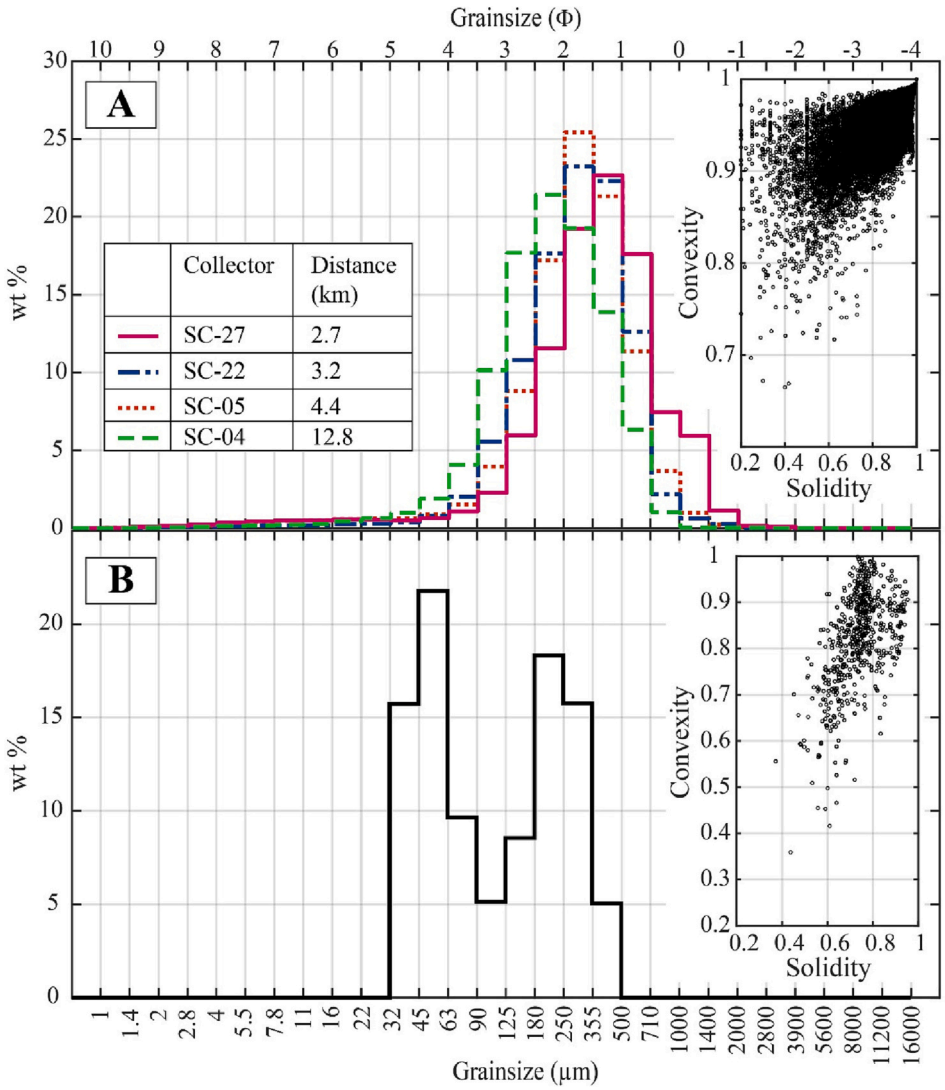

Fig. 5. A. GSDs of the tephra accumulated in tephra collectors (sab. samples) for the different locations in wt%. The inset on the right shows the shape parameters, convexity and solidity, of tephra sampled in tephra collectors. B. GSD of primary tephra samples (prim. samples) collected on adhesive paper at sites 25–28 (4.4 km from the vent). The inset shows the convexity and solidity of primary tephra particles collected on adhesive paper.

tephra collectors is 1560.1 ± 26.9 kg m^{-3}.

GSDs of primary tephra collected on adhesive paper are bimodal, with fine (45–63 μm) and coarse (180–250 μm) modes (Fig. 5B). Traces of volcanic ash aggregates are found on adhesive paper samplers, which most likely correspond to the particle clusters described by Brown et al. (2012) and Bagheri et al. (2016) that easily break up upon impact. Solidity and convexity of the particles in the fine and coarse modes are between 0.57 and 0.90 and 0.63 and 0.97, for 90% of particles, respectively (Fig. 5B).

4.3. Volume of tephra deposits

An isopach map was compiled from the cumulative thickness of layers A and B (Fig. 6A) in order to constrain the volume emitted between the beginning of the eruption and the field campaign (i.e., from November 2016 to August 2018). In fact, as mentioned above, both layers A (with constant thickness) and B (with decreasing thickness away from vent) are interpreted as deposits from the current eruption, with the only difference that layer A is continuously remobilised as it represents the most surficial layer. Unfortunately, the number of available field sites was spatially limited, because it was not possible to access the western part of the volcano. The deposit is elongated *E*-W, in agreement with the prevailing wind directions during the dry and wet seasons, respectively (Fig. 1B; Thouret et al., 1994). The gradual decrease of the deposit thickness with distance was fitted with exponential, power-law and Weibull trends (Fig. 6B). The details of the different fitting strategies are described in Appendix C. For the power-law fitting, an exponent $m < 2$ ($m = 1.2$) is found, which is characteristic of poorly exposed deposits; and the estimate of the volume is, therefore, sensitive to the distal integration limit (Bonadonna et al., 2015; Biass et al., 2019). In order to account for this sensitivity and provide uncertainties on volumes obtained from the power-law fitting strategy, the volume was calculated by averaging the estimates for two different distal integration limits that correspond to the values of the square root areas at which the thickness predicted by power-law trend is equal to 0.01 and 0.001 cm (i.e., thickness becomes comparable to the diameter of individual fine particles).

The estimated volume of tephra deposits is 0.03 ± 0.01 km^3, 0.06 ± 0.03 km^3 and 0.03 ± 0.02 km^3 with the exponential, power-law and Weibull fitting strategies, respectively. Based on the average of these estimates, we determined that a volume of 0.04 ± 0.02 km^3 was deposited between November 2016 and August 2018. This corresponds to a total DRE volume of 0.02 ± 0.01 km^3 calculated from the values of the deposit and DRE densities presented above. On average, over this

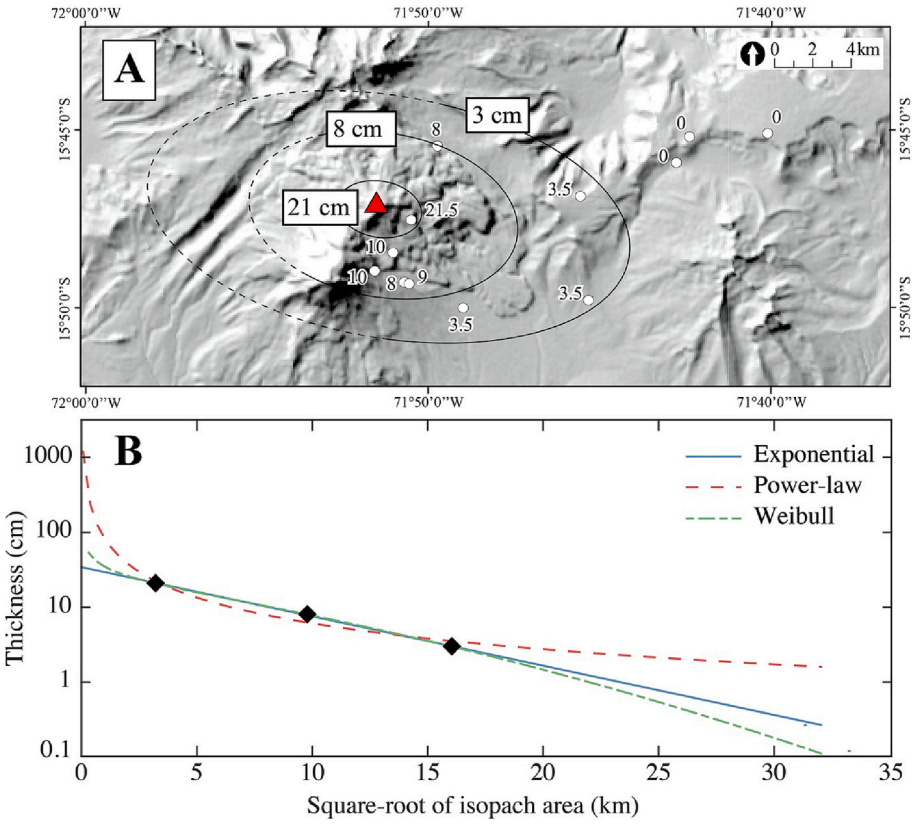

Fig. 6. A. Isopach map (in cm) of layers A and B combined (thickness measured in August 2018). The position of the vent is indicated by the red triangle. B. Semi-log plot of the deposit thickness against the square-root of isopach areas. Exponential, power-law and Weibull fits are represented by the solid blue, dashed red and dashed-dotted green lines, respectively. Uncertainties of 30 and 40% were assumed for thickness and area estimations, respectively.

entire period, a DRE volume of $1.1 \pm 0.5 \times 10^{-3}$ km^3 was produced each month.

4.4. Mass of tephra collected in tephra collectors

A map of the average tephra mass load deposited each month between April 2018 and November 2019 was compiled from the data of the tephra collectors (Fig. 7A). The number of data points available is limited, and we were only able to estimate three contours, which are poorly constrained southwest of the vent, in the area that lacks tephra collectors. The elongation of the contours suggests tephra dispersion towards the east-southeast and the west-northwest, in agreement with the dispersal of the ground tephra deposit (Fig. 6A). The gradual decrease of the monthly accumulated tephra load with distance was also fitted with exponential, power-law and Weibull trends (Fig. 7B; Appendix D). Again, m (see Appendix C) is found to be below 2 ($m = 1.7$) for the power-law fitting, indicating that the estimation of the monthly accumulated mass is sensitive to the distal integration limit. Hence, the mass was calculated by averaging the estimates for two distal integration limits that correspond to the values of the square root areas at which the power-law thickness equals 0.1 and 0.01 kg m^{-2}.

An average mass of $6.8 \pm 3.5 \times 10^7$ kg per month is obtained using the exponential function, $6.1 \pm 2.8 \times 10^7$ kg per month with the power-law function and $6.2 \pm 2.7 \times 10^7$ kg per month with the Weibull function. From the average of the results obtained with the different fitting strategies, we therefore arrived at a monthly accumulated mass of $6.5 \pm 3.1 \times 10^7$ kg per month for the period from April 2018 to November 2019. Using the deposit and the DRE densities, this corresponds to a DRE volume of $2.3 \pm 1.1 \times 10^{-5}$ km^3 produced each month.

4.5. Pulsatory explosive activity of Sabancaya

Eruptive activity at Sabancaya has been characterised by a cyclic and pulsatory eruptive style since November 2016, when the first magmatic explosions took place. A detailed statistical analysis and the application of the renewal log-logistic model to describe the temporal variation of the repose time between explosions allows the quantification of the unsteadiness of this activity (see Appendix B). Variations of the pulsatory activity are correlated with the 6 eruptive phases identified by Coppola et al. (2022) between November 2016 to December 2020 (Table 4). As shown in Fig. 8A, phase II, previously defined by Coppola et al. (2022) as an intense explosive activity accompanied by dome growth, was sub-divided into three stationary sub-phases (IIa, IIb and IIc), defined as periods for which the probability distribution of the repose interval is constant in time, implying homogeneous eruptive styles. Indeed, the phase II was characterised by 3 deepening-refilling cycles marking variations in frequency and energy of explosions by Coppola et al. (2022).

The results of the detailed repose interval analysis show an alternation of low (i.e., phases I, V, VII) to medium frequency (i.e., phases IIb, III, IVa, IVb, IVc, VI) activity, with high frequency phases (i.e., IIa, IIc, IVd, VIII). In fact, phases I, V and VII, with 11, 10 and 6 explosions per day, represent the lowest frequency phases with variable median repose times of 70, 25 and 80 min, and large maximum repose times of 38, 222 and 68 h, respectively. The phases with higher frequency (IIa, IIc, IVd, VIII), with 38, 42, 55 and 42 explosions per day also have the shortest median repose times, between 18 and 23 min, and variable maximum repose times of 39, 29, 6 and 9 h, respectively (Table 4). During the field campaign in July–August 2018, an average of 21 explosions per day, with a median repose interval of 41 min, were recorded (Fig. 8A, Table 4).

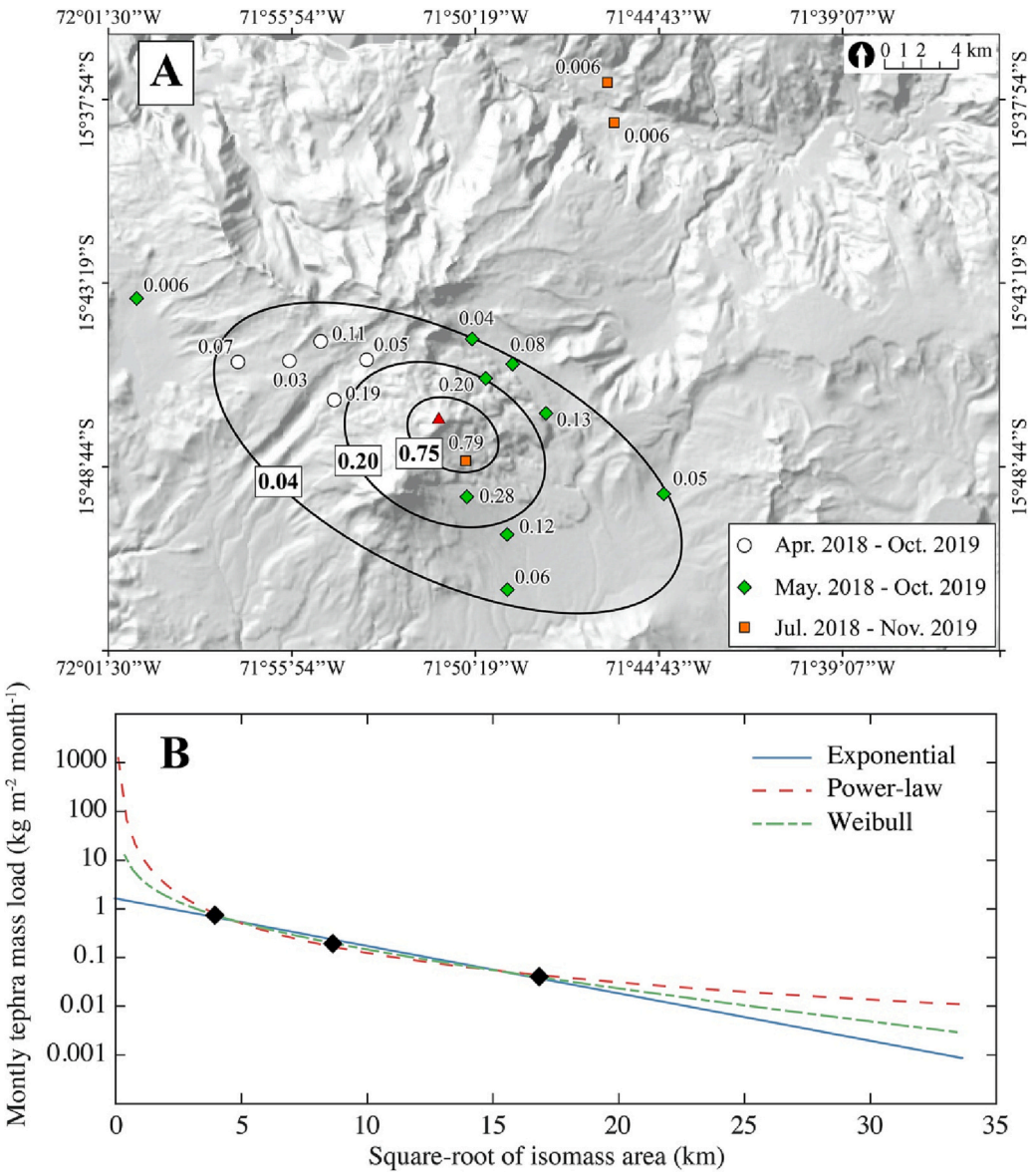

Fig. 7. A. Isomass map in kg m^{-2} $month^{-1}$ for the average monthly accumulation of tephra in tephra collectors from April 2018 to November 2019. Sampling from three overlapping periods has been considered together in order to draw the isolines: from April 2018 to October 2019 in the white circles, from May 2018 to October 2019 in the green diamonds and from July 2018 to November 2019 in the orange squares. The position of the vent is indicated by the red triangle B. Mass decay profile computed from the isomass map in a semi-log plot of the tephra accumulation against the square root of isomass areas. Exponential, power-law and Weibull fits are represented by the solid blue, dashed red and dashed-dotted green lines, respectively. Uncertainties of 30 and 40% were considered for mass load and area estimations, respectively.

Table 4
Repose time interval (median, mean and maximum values) and log-logistic parameters (μ and s) for all the phases analysed at Sabancaya from 2016 to 2021. The period of the field campaign is also described.

Phase	Start date (DD/MM/YYYY)	End date	Median (min)	Mean (min)	Maximum (hours)	Frequency (explosions day^{-1})	μ	s
I	06/11/2016	23/12/2016	70	132	38	11	8.36	0.65
IIa	24/12/2016	24/03/2017	23	38	39	38	7.17	0.58
IIb	25/03/2017	25/08/2017	34	54	86	27	7.53	0.63
IIc	26/08/2017	23/01/2018	25	34	29	42	7.23	0.58
III	24/01/2018	13/03/2019	51	88	44	17	8.02	0.61
IVa	13/03/2019	11/05/2019	38	70	24	21	7.71	0.64
IVb	12/05/2019	31/07/2019	39	83	35	18	7.75	0.71
IVc	1/08/2019	25/09/2019	34	55	17	27	7.55	0.64
IVd	26/09/2019	23/10/2019	18	27	6	55	6.96	0.57
V	23/10/2019	30/08/2020	25	138	222	10	7.41	0.85
VI	01/09/2020	30/11/2020	35	56	13	26	7.62	0.62
VII	01/12/2020	02/02/2021	80	235	68	6	8.53	0.89
VIII	03/02/2021	05/05/2021	23	34	9	42	7.16	0.59
Field campaign	27/07/2018	12/08/2018	41	62	19	21	–	–

Based on the median of the repose time and the magma viscosity correlation proposed by Dominguez et al. (2016), the 2 phases for which it was possible to estimate the magma viscosity (i.e., phases IIb and III; Fig. 8B) follow the trend of other Vulcanian pulsatory activities with similar compositions, such as the 2003 cycle of Santiaguito (Guatemala). The log-logistic parameters of the repose interval distribution (see

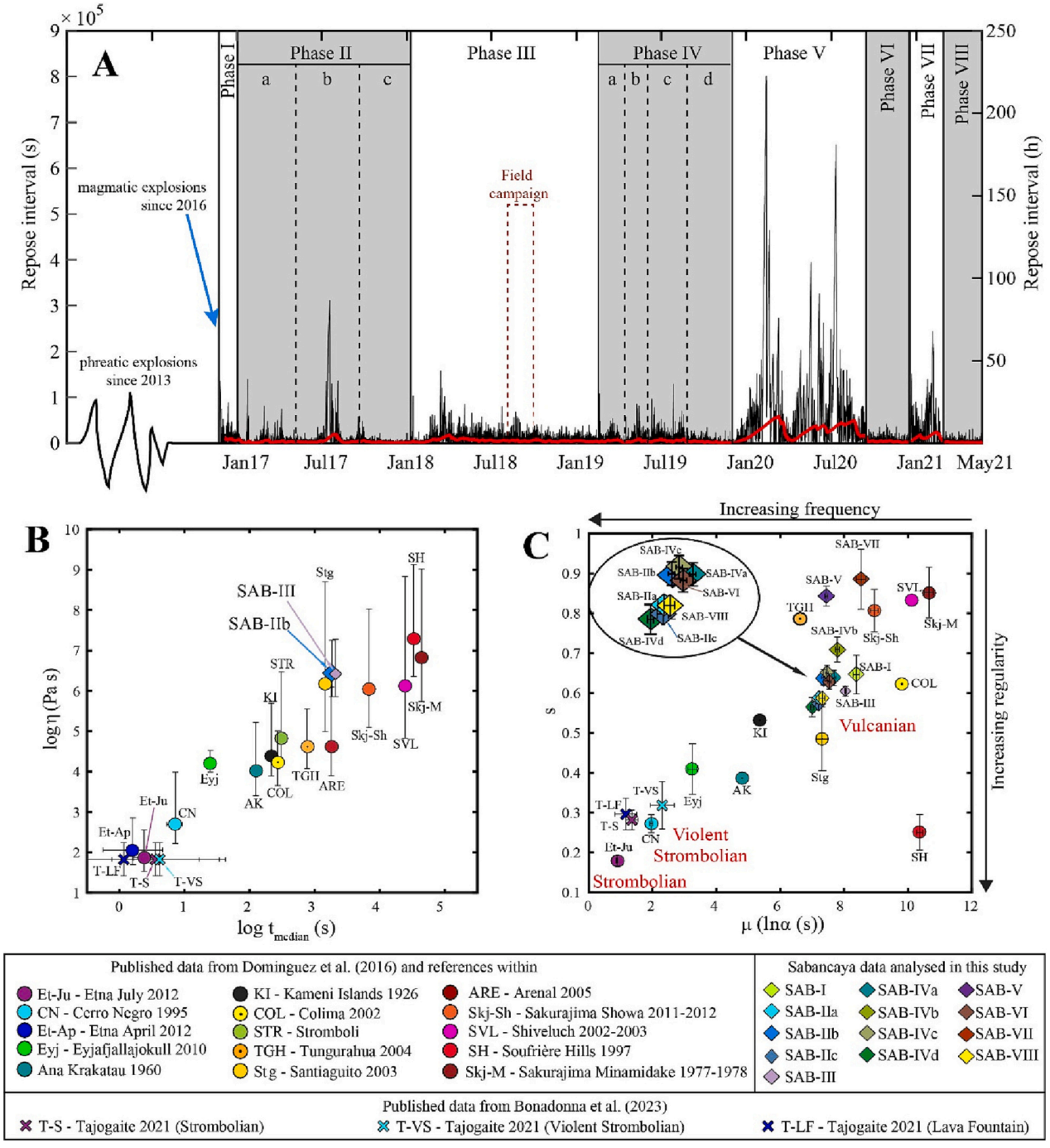

Fig. 8. A. Time series of explosions at Sabancaya from the beginning of the eruption up to May 2021 shown by the repose interval between explosions. The red solid line corresponds to the moving-average of the repose interval, calculated based on 20 data points. Based on the work of Coppola et al. (2022) and the variability of the time series, 8 phases have been identified. The dashed red box indicates the time of our field campaign. B. Variations of magma viscosity as a function of the median of the repose interval for several published data and for the phases IIb and III of Sabancaya where viscosity has been estimated. C. Classification of pulsatory activity based on the log-logistic parameters for the distribution of the repose time interval, μ and s, associated with the frequency and regularity of activity, respectively. Circles correspond to various eruptions of the dataset of Dominguez et al. (2016). Diamonds correspond to the eight phases of Sabancaya analysed in this study.

Appendix B), μ (associated with α, the scale of the distribution) and s (associated with the shape of the distribution), which provide insights into the frequency and regularity of activity, respectively, are summarised in Table 4 and shown in Fig. 8C for all the phases identified at Sabancaya, and compared with a dataset of various pulsatory eruptions (Dominguez et al., 2016). Highest frequency phases (i.e., IIa, IIc, IVd, VIII) are clustered with the lowest μ and s, indicating phases of frequent and regular activity; whilst the medium frequency phases (i.e., IIb, III, IVa, IVb, IVc, VI) are clustered with a slightly higher μ and s. In contrast, the lowest frequent phases (i.e., I, V, VII) show a high variation in μ and s corresponding also to the high variation of the median of the repose interval and the irregularity of this activity, particularly for the phases V and VII with the highest values of s (Fig. 8C). All Sabancaya phases correspond to Vulcanian style in the μ vs s plot.

4.6. Tephra remobilisation

A variety of syn-eruptive aeolian remobilisation phenomena were encountered during the field campaign. These phenomena can be described using the classification of Dominguez et al. (2020b), which has been adapted from the lithometeors of the World Meteorological Organization and is based on the loss of visibility (Fig. 9). Here, we focus on the class of phenomena that describes particles being raised in the atmosphere at the time of observation. We do not describe phenomena that correspond to particles already suspended prior to the time of observation.

Drifting and blowing ash consist of ash raised by the wind to low (<1.80 m) and moderate (~1.80 m) heights, respectively, for durations on the order of minutes (Fig. 9A-B; Supplementary Video 1). They are the most common remobilisation phenomena that were daily observed under all weather conditions.

Ash whirls (also called "ash devils") share similarities with drifting and blowing ash, but with ash being raised in the form of a column that spins around an approximately vertical axis (Fig. 9C; Supplementary Video 2). The formation of ash whirls is powered by heating from insolation and their lifetime spans between tens of seconds and a few minutes (Sinclair, 1969; Balme and Greeley, 2006). They were repeatedly observed in the field, with multiple ash devils observed daily.

Finally, ash storms are the most intense and rarest remobilisation phenomenon that were encountered only during 2 consecutive days in the field. Large quantities of ash are lifted to great heights (100s or 1000s of metres) by strong turbulent winds and visibility is greatly reduced (Fig. 9D; Supplementary Video 3). Ash storms can raise particles for prolonged periods of time (days) and trigger ash hazes (i.e., particles suspended in the atmosphere), even far from the source.

4.7. HS videos and PM_{10} measurements

The remobilisation transport mechanisms were imaged at the scale of the particles. The remobilisation of the grains was intermittent, with short periods of gusts during which numerous particles were seen in motion separated by longer periods of rest. HS videos additionally offer an insight into the different remobilisation mechanisms, with coarse particles moving by creep on the ground surface, and finer particles transported by saltation (see Supplementary Video 4). While the resolution of the images was not sufficient to image the very fine particles that have the potential to enter into suspension, the splash effect was observed during aeolian remobilisation events, when saltating particles hit the surface and trigger the motion of other particles upon impact, favouring their remobilisation and potential entrainment into suspension (Shao et al., 1993; Supplementary Fig. S5).

As seen in the HS videos, short-lived wind gusts can entrain numerous particles in suspension that were also evidenced in the PM_{10} concentration measurements. Temporal variations in the PM_{10} series show the intermittent nature of aeolian remobilisation (Fig. 10), with concentrations that tend to increase over the course of the day, in correlation with the diurnal evolution of soil surface and meteorological properties (Mingari et al., 2020). Specifically, an increase in PM_{10} concentration is associated with an increase in the wind speed and the surface temperature over the course of the day (Fig. 10). Average PM_{10} concentrations vary as a function of the date and location but tend to be higher for the days when ash storms were reported (Table 4). PM_{10} values are rarely above the limit of 0.45 mg m^{-3} defined by the World Health Organization for daily average exposures (World Health Organization, 2021), with only one day (04 August 2018) for which it was measured to be higher than 0.45 mg m^{-3} over a short duration of 1 h and 11 min.

4.8. Characterisation of remobilised ash

Fig. 11 shows the GSDs of airborne remobilised particles collected on adhesive paper at ground level (R0) and at heights >1.5 m (R150) (see Fig. 3 that illustrates the differences between the sampling strategies). It is clear that the GSDs are distinct, possibly due to the different transport mechanisms of the particles. R0 samples are associated with a fine modal diameter of 45–63 μm, whilst R150 samples exhibit a very fine mode at 11–16 μm (red and blue GSDs of Fig. 11, respectively).

In order to better understand these differences in the sizes of remobilised particles, the GSDs of airborne remobilised particles are

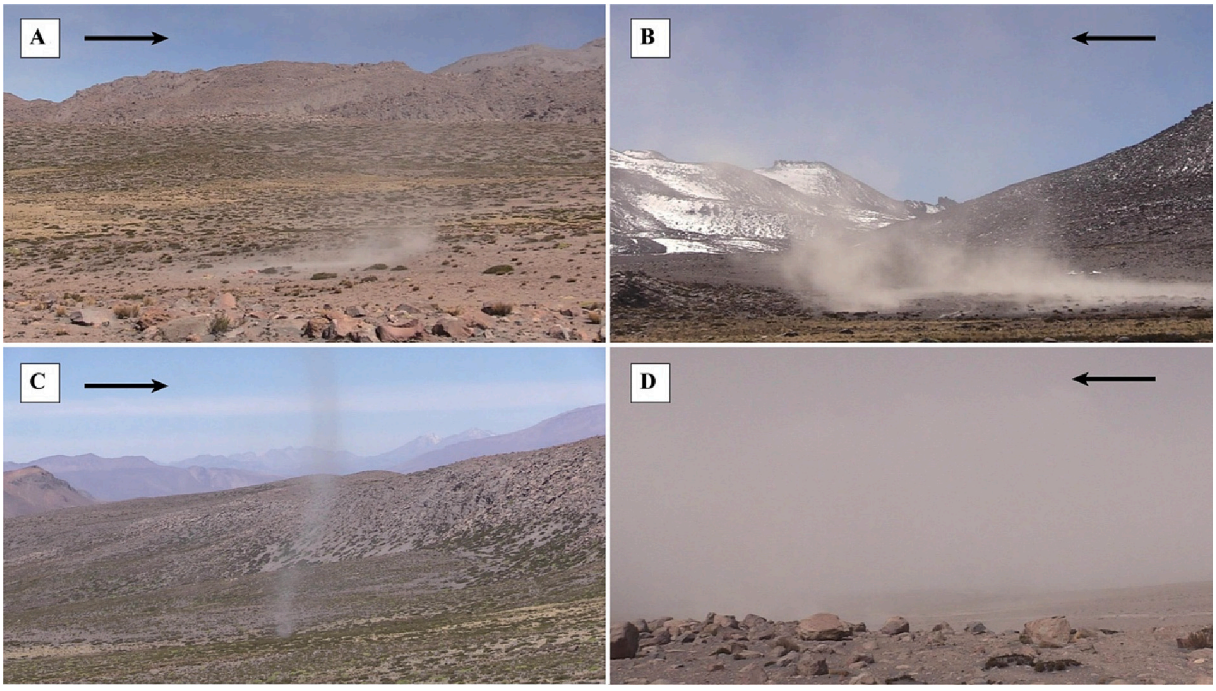

Fig. 9. Aeolian remobilisation phenomena observed at Sabancaya during the field campaign (from 27 July to 12 August 2018). A. Drifting ash on 30 July 2018 B. Blowing ash on 30 July 2018 C. Ash whirl on 30 July 2018 D. Ash storm on 03 August 2018. Black arrows point in the direction of the wind.

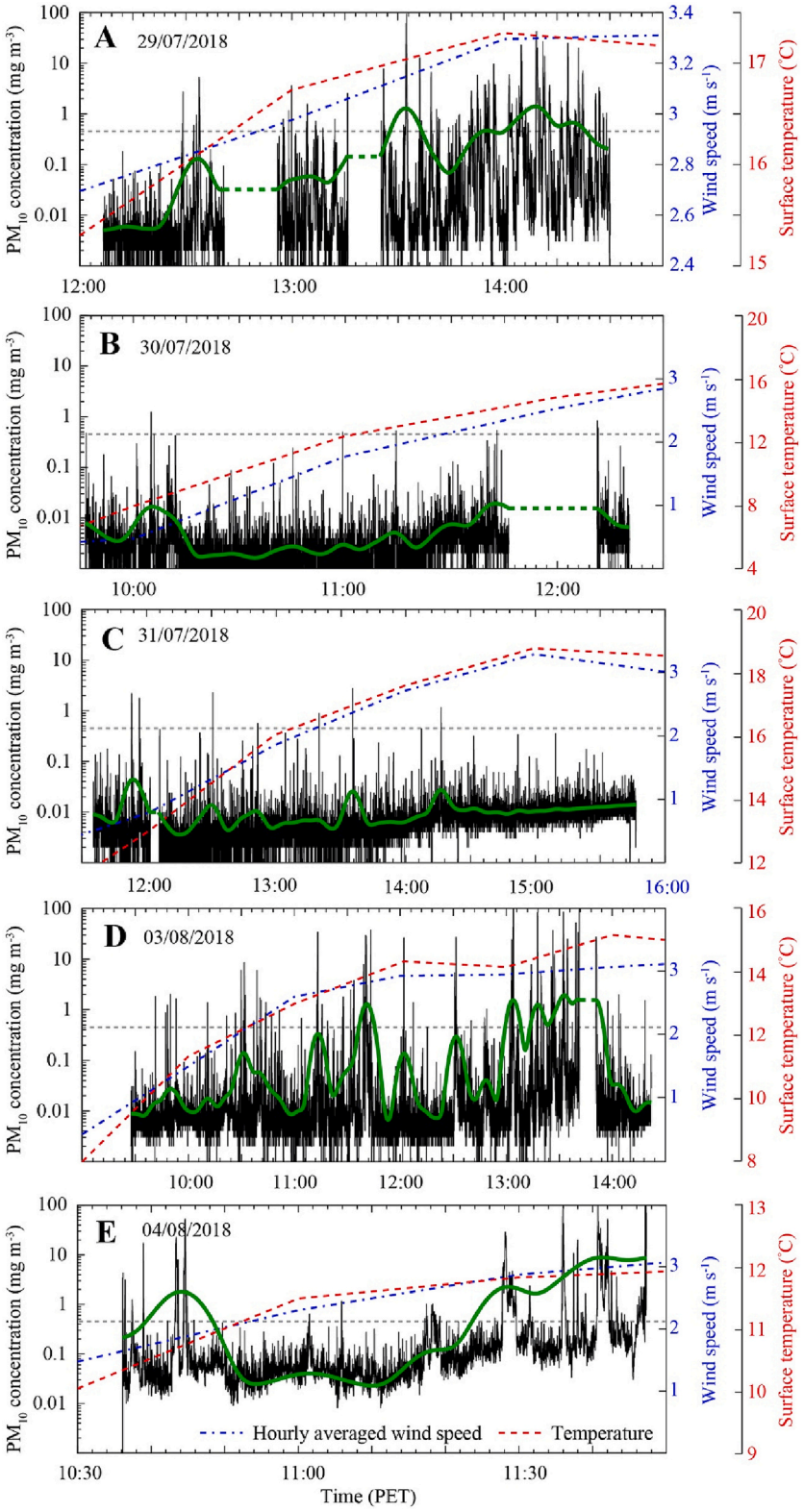

Fig. 10. PM_{10} concentration measurements for A. 29 July, B. 30 July, C. 31 July, D. 03 August and E. 04 August 2018 compared with hourly averaged wind speed at 10 m above the surface (dashed-dotted blue line) and temperature (dashed red line) obtained from the ECMWF ERA-Interim reanalysis. The solid green line is the moving average of the PM_{10} concentration, calculated using a 2-min window. Dashed grey lines indicate the 24 h air quality guidelines of 0.45 mg m^{-3} (World Health Organization, 2021). PM_{10} measurements were performed at different locations indicated in Table 2 and the inset map of Fig. 2B. Table 2 contains additional information on PM_{10} measurements (i.e., duration, average concentration and observations of remobilisation phenomena).

compared with the sample of the most surficial ground layer collected upwind, which is representative of the source material (SG sample; Fig. 11). Volcanic ash particles on the ground are coarser than airborne remobilised ash, with a modal diameter of 250–355 μm. This indicates that aeolian remobilisation is a size-selective process favouring the transport of fine particles, as already described in a number of studies (Shao and Lu, 2000; Kok et al., 2012; Jarvis et al., 2020).

The GSDs of remobilised and ground particles are additionally compared with the threshold friction velocity model, u_{*_t}, of Shao and Lu (2000) and the model of Mingari et al. (2020) for transport mode (Fig. 11). R0 samples are associated with the grainsizes that minimise the threshold friction velocity, typically between 70 and 100 μm. Hence, they correspond to the particles that are most likely moving only under action of the wind, whilst both coarser and finer particles are

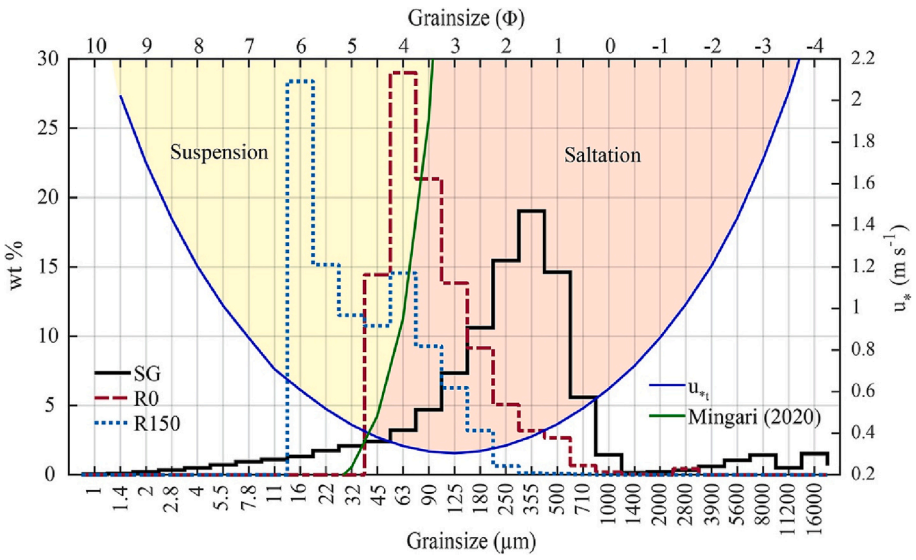

Fig. 11. Representative GSDs of the most surficial ground layer (SG) upwind of airborne particles remobilised by the wind sampled at ground level (R0) and at heights >1.5 m (R150). Samples have been collected at sites 31, 40, and 61, respectively at 4.1, 4.5 and 4.4 km from the vent (Supplementary Table 1). The GSDs are compared with the model of the threshold friction velocity (u_{*t}) of Shao and Lu (2000) (solid blue line) indicating the minimum wind friction velocity (u_*, on the right y-axis) for which grains become mobile and the model of Mingari et al. (2020) (solid green line) showing the critical grainsize at which a transition between suspended and saltating particles might occur. The yellow and orange shaded regions respectively cover the grainsizes that are transported in suspension and saltation for $u_* > u_{*t}$.

respectively too heavy and too cohesive to easily lift off. Considering low and common wind friction velocities ≤0.5 m s^{-1} (Dominguez et al., 2020a; Mingari et al., 2020), the particles collected on R150 samples are unlikely to be remobilised only by the wind, but rather due to the impact of coarser saltating particles with the ground (Shao et al., 1993). Moreover, for the same range of wind friction velocities, particles with diameters below the range 32–45 μm are expected to stay in suspension once in the atmosphere, as their settling velocities are lower than the wind friction velocity (Mingari et al., 2020). This size threshold is found to correctly separate the modal grainsize of particles collected on R0 and R150 samples (Fig. 11).

The morphologies of airborne primary (prim.) and remobilised (R0 and R150) particles collected on adhesive paper are presented in Fig. 12. Similarly to Dominguez et al. (2020b), we refined the shape analysis by separating the particles into three size classes: (i) below 63 μm (class 1), (ii) between 63 and 125 μm (class 2), and (iii) above 125 μm (class 3). In general, the shape descriptors of primary and remobilised ash exhibit differences in the median values of <0.1 (Fig. 12). Nonetheless, specific statistical tests performed on these populations suggest that significant differences exist between the shape of primary and remobilised particles (Supplementary Table S3). For classes 1 and 2, the shape descriptors characterising primary particles are different to those of R0 samples, but statistically equivalent to those of R150 samples. For class 3 particles, differences exist between primary and remobilised particles of R0 and R150 samples. Subtle, but significant, differences in the shape descriptors of R0 and R150 samples exist for all classes. Remobilised particles of R150 samples from classes 1 and 3 are additionally associated with more variability in the shape descriptors than primary ash (Fig. 12), as supported by the results of Levene-tests indicating heterogeneous variances for all tested shape descriptors (Supplementary Table S3).

In more detail, for classes 1 and 2, the median values of shape descriptors are significantly greater for R0 samples than for primary particles. For example, the median form factor of remobilised particles ≤125 μm within R0 samples is 0.52 for both class 1 and class 2, whilst the form factor of primary ash particles is 0.45 and 0.46, for classes 1 and 2, respectively. The form factor and solidity of class 3 R0 and primary particles are slightly dissimilar, with differences in median values of <0.03, whilst the values of convexity are statistically equivalent. The means of the shape parameters describing particles from R0 and R150 samples are significantly greater in all classes. This suggests that particles within R0 samples are slightly rounder and smoother than primary particles and particles within R150 samples. The shape of primary particles is similar to that of R150 samples, except for class 3 particles, for which the median of all shape parameters is slightly greater for primary particles, with differences in median values of approximately 0.03–0.04.

5. Discussion

5.1. Preservation and interpretation of tephra deposits

Tephra deposits retain valuable information into the dynamics of past eruptions and are used to reconstruct the total GSD, magnitude, intensity and duration of volcanic events (e.g., Bonadonna et al., 2015 and references therein). They are, therefore, key to compile hazard and risk assessments as well as to better understand the plumbing system of a volcano (e.g., Bonadonna et al., 2016, 2021 and references therein). Unfortunately, post-depositional processes such as aeolian remobilisation can affect the characteristics of the deposits (Engwell et al., 2013), especially in cyclic volcanic contexts during which low quantities of tephra are produced intermittently in very dynamic erosional conditions.

Based on stratigraphic analysis, 5 main tephra layers were distinguished at Sabancaya. At distances <10 km from the vent, the most superficial layers A and B can be related to the ongoing activity (post-2016), whilst layer C can be associated with the previous eruptive cycle. Further from the vent, tephra deposits consist in only two layers (D1 and D2) that could not be related to any recent eruption at Sabancaya volcano given that they may represent older eruptive phases or possibly underwent intense reworking processes.

Both layers A and B show clear evidence of wind reworking. According to field observations, the loose layer A that constitutes the very top of the stratigraphic sections is subject to continuous deposition of primary tephra and simultaneous subsequent remobilisation. The thickness of layer A does not decrease with distance from the vent and is rather homogeneous for the entire area studied during the field campaign (Fig. 4, Supplementary Table S1), as it corresponds to the uncompacted tephra deposit that is continuously being remobilised and redistributed over the area surrounding the vent (Dugmore et al., 2020). In these arid areas of low vegetation cover, the deposit thickness is particularly sensitive to local variations in the windward and leeward sides of plants, and it is a result of tephra entrapment and preservation in the vegetation during primary and secondary transport (Blong et al., 2017; Dugmore et al., 2018; Dominguez et al., 2020b). It is worth mentioning that additional water and glacial erosion take place at

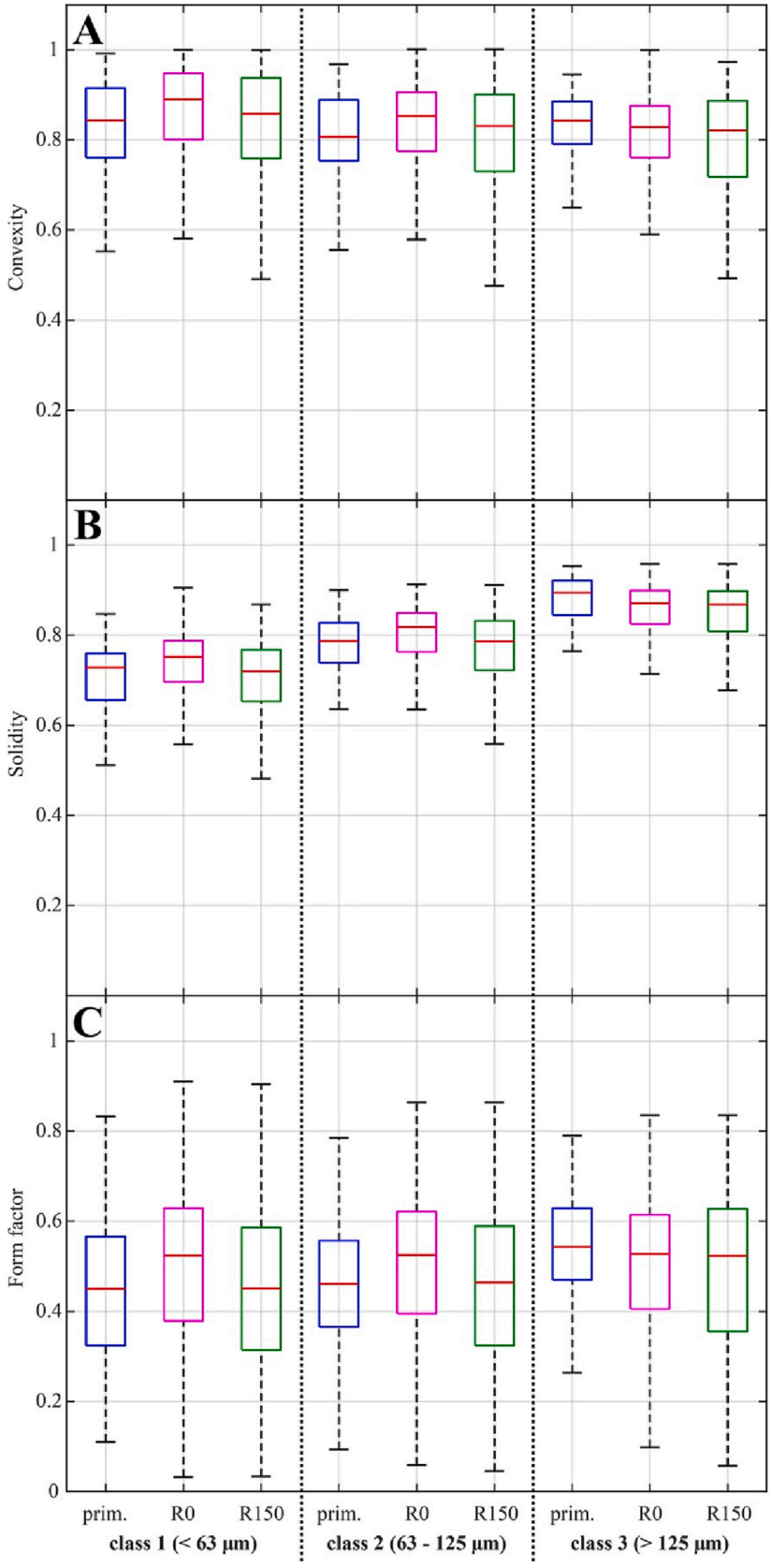

Fig. 12. Box and whisker plots showing the comparison of A. convexity, B. solidity and C. form factor between airborne primary (prim.) and remobilised (R0 and R150) ash particles collected on adhesive paper. Values close to 1 in these shape descriptors are indicative of smooth and rounded particles.

Sabancaya as well (Thouret et al., 1994). As a consequence, the interpretation of stratigraphic sections could lead to inaccurate assessments of the eruptive parameters, and should be complemented by different sampling methods (e.g., ground and airborne material, vertical and horizontal mass fluxes), field observations (e.g., HS and high-resolution videos) as well as measurements in various environments (e.g., including sections in peat bogs; Juvigné et al., 2008; Fontijn et al., 2014). Only such a multifaceted study will enable a comprehensively constraining the tephra layers of pulsatory activity in dynamic weather terrains, as is the case of Sabancaya.

5.2. Volume of tephra deposits

Based on measurements of the deposits thickness, it is estimated that a DRE volume of 0.02 ± 0.01 km^3 was emitted between November 2016 and August 2018 (Fig. 6). This volume is comparable to the volume of 0.025 km^3 emitted from May to October 1990 during the previous eruption of Sabancaya (Thouret et al., 1994; Gerbe and Thouret, 2004), even though it was emitted over 2 years. The volume of tephra deposits estimated here corresponds to an average volume of $1.1 \pm 0.5 \times 10^{-3}$ km^3 DRE emitted each month. This is two orders of magnitude greater than the DRE volume of $2.3 \pm 1.1 \times 10^{-5}$ km^3 per month obtained from the mass accumulated in the tephra collector network, between April 2018 and November 2019, suggesting a significant decrease in the tephra production rate after the start of the eruption. In fact, the measurements of Coppola et al. (2022) also suggest that considerably smaller volumes of tephra have been emitted since 2018. The cumulative volume estimated for the period from November 2016 to December 2020 is 0.004–0.009 km^3 DRE (Coppola et al., 2022), corresponding to an average DRE volume of $1.3 \pm 0.7 \times 10^{-4}$ km^3 per month, which is between and consistent with the estimates above, as both the start and the post-2018 phase of the eruption are taken into account.

It is also possible to compare these values with the amount of tephra produced by Vulcanian eruptions at other volcanoes. The volume of tephra produced by Sabancaya is low in comparison with the large Vulcanian explosions of Soufrière Hills volcano (Montserrat), for which the average tephra volume per explosion was estimated at 1.0×10^{-4} km^3 from August to October 1997 (Bonadonna et al., 2005; Druitt et al., 2002). The size, magnitude and frequency of the explosions at Sabancaya are instead more comparable to their counterparts at Sakurajima volcano. Between 2011 and 2015, Oishi et al. (2018) estimated the averaged volume of volcanic ash fallouts to range from 3×10^{-4} to 4×10^{-4} km^3 per month. These values are similar to those estimated at Sabancaya for the period between November 2016 and August 2018 (average of $9.1 \pm 4.5 \times 10^{-4}$ km^3 DRE per month), and one order of magnitude higher than the volumes emitted between April 2018 and November 2019 (average of $2.9 \pm 1.3 \times 10^{-5}$ km^3 per month).

5.3. Vulcanian activity at Sabancaya volcano

The current eruptive cycle at Sabancaya is characterised by a Vulcanian eruptive style, as suggested by the repose time analysis of the whole cycle from 2016 to 2021 (Fig. 8; Table 4). Explosive activity displays significant temporal variations regarding the frequency and the regularity of explosions, from which at least 8 phases have been identified. In general, there is an intercalation of low and high frequency phases, suggesting significant changes in fragmentation processes that might be affected primarily by the extrusion and growing of domes, interplay among magma feeding and degassing, inducing changes in the magma rheology and ascent dynamics, overpressure in the conduit and shearing effects, or variable interactions with surface waters (Gonnermann and Manga, 2012; Pistolesi et al., 2021; Gerbe and Thouret, 2004). The analysis of the magma viscosity and the median repose time between explosions shows a robust correlation for the phases IIb and III, following the trend of similar dacitic compositions such as the 2003 Santiaguito cycle (Fig. 8B). Unfortunately, we were not able to constrain the effect of viscosity on the other phases which might play an important role on the construction and collapse of domes described at Sabancaya. Coppola et al. (2022) demonstrated that at least 3 phases have been associated with the growing of two domes (i.e., the "Huk" dome during phases II and IV and the "Iskay" dome during phase VI). The periodicity at which the dome growth was observed for the phases II, IV and VI is consistent with high frequency explosive phases with low median repose intervals between explosions (18 to 35 min; Table 4). Similarly, the collapse of the "Huk" dome during phase V (Coppola et al., 2022) is associated with the lowest frequency period for the ongoing explosive cycle, associated with a median repose time of 25 min but with maximum intervals between explosions of up to 222 h.

In addition, the log-logistic parameters, μ and s, of the repose time distributions show that explosions in different phases of Sabancaya's activity are as frequent as the 2003 Santiaguito and the 2011–2012 Sakurajima-Showa cycles, but with less regular behaviour (Fig. 8C). As observed by Dominguez et al. (2016) for other pulsatory volcanoes, the frequency of explosions decreases as μ increases and the regularity of the activity decreases with s. In the case of Sabancaya, we can see that the 8 phases follow a general linear trend between μ and s, within the range of Vulcanian activity (Fig. 8C). In particular, the most frequent phases IIa, IIc, IVd and VIII, are as frequent as the 2003 Santiaguito activity but less regular; whilst the medium frequency phases IIb, III, IVa, IVb, IVc and VI are slightly less regular still. The phase V, associated with the collapse of the "Huk" dome shows similar values of regularity to the 2011–2012 Sakurajima-Showa activity, but with more frequent explosions (Fig. 8C). The cyclic eruptive processes of Sabancaya are correlated with complex effusive and explosive dynamics controlled by the growing and collapse of domes, the magma-rise rate and fragmentation processes consistent with frequent but irregular Vulcanian eruptive styles.

5.4. Characteristics of remobilised material and identification of primary tephra

Aeolian remobilisation at Sabancaya is recurrent during the day and takes multiple forms from low intensity events, such as drifting ash, to strong turbulent ash storms (Fig. 9). These observations are consistent with the aeolian reworking features found in tephra deposits. Field observations and PM_{10} concentration measurements suggest the possible control of diurnal weather variations on aeolian phenomena, but longer measurements (i.e., 24 h) are required to confirm these preliminary trends. The concentration of suspended material typically increases as the day progresses and surface conditions evolve (e.g., increase in wind velocity and surface temperature) (Fig. 10). For all the days during which PM_{10} data were acquired, concentrations rarely exceeded air quality guidelines. The PM_{10} concentration was higher in ash storms (Table 2; Fig. 10D-E), exceeding 0.45 mg m^{-3} over periods of 30 to 45 min, but more investigation is required to monitor the average over 24 h. In fact, these exploratory measurements necessitate further analysis to evaluate if the remobilisation of volcanic ash constitutes a respiratory hazard at Sabancaya, but also in the populated Colca river valley.

Differential sampling of airborne remobilised ash at the ground level (R0) and above 1.5 m (R150) (Fig. 3) shows that the GSDs depend greatly on the transport mechanism (Fig. 11). Consistently, R0 samples are associated with a grainsize mode of 45–63 μm that minimises the threshold friction velocity as defined by Shao and Lu (2000). We can therefore estimate that R0 samples are associated with a predominant saltation (i.e., bouncing) mechanism. For probable wind friction velocities $\leq$0.5 m s^{-1} (Dominguez et al., 2020a; Mingari et al., 2020), these particles are characterised by relatively high settling velocities compared to the wind friction velocity. On the other hand, particles collected on R150 samples are finer, with a mode $<$20 μm. These particles are characterised by grainsizes having settling velocities significantly lower than probable wind friction velocities, on the order of 0.3 to 0.5 m s^{-1} (Mingari et al., 2020). It is therefore likely that these particles were already in the atmosphere at the moment of collection and that

they possibly underwent short- to long-term resuspension. Despite the fact that we were not able to measure friction and settling velocities, the simple sampling strategy developed here for collecting airborne remobilised material in real-time (Fig. 3) represents a suitable technique to separately analyse saltating and suspending particles and the associated transport features.

Finally, even though the shape descriptors of fine particles <63 μm are calculated for low pixel densities <750 px per particles, which limits the accuracy of morphological analysis for class 1 particles, statistically significant distinctions in the morphologies of primary and remobilised tephra are found. This is similar to other examples of remobilised deposits analysed some years after primary depositions (e.g., eruption of Cordón Caulle, Chile, in 2011–2012; Dominguez et al., 2020b). In fact, for the case of Cordón Caulle, tephra was deposited in Patagonia mostly in June–July 2011 (total volume about 1 km^3; Pistolesi et al., 2015) and subsequently remobilised over years. Morphological analysis of primary tephra particles and remobilised ash then allowed the distinction of the two populations of grains, with remobilised particles significantly rounder and smoother than the primary material because of abrasion due to secondary transport over several months and even years (Dominguez et al., 2020b). In the case of Sabancaya, where primary production of tephra and aeolian remobilisation occur simultaneously, remobilised particles exhibit slightly rounder morphologies than the primary tephra. We find variations indicating that remobilised ash ≤125 μm collected in R0 samples (i.e., probably transported by saltation) are slightly more circular and smoother than primary ash (Fig. 12; Supplementary Table S3). In fact, particles that undergo saltation experience regular collisions that result in abrasion and rounding of the particle surfaces. Although the difference in the shape descriptors is less pronounced at Sabancaya, this is in agreement with the results of Dominguez et al. (2020b), who demonstrated the rapid abrasion of remobilised volcanic ash in Patagonia, less than five years after the eruption of Cordón Caulle, particularly for sizes prone to saltation (63–125 μm), and consequently easier to be remobilised. For sizes >125 μm, particles from R0 samples have more similar morphologies compared to primary ash, as they are too heavy to be easily remobilised by the wind and undergo less abrasion. The particles collected in R150 samples are more likely to be transported by suspension with fewer collisions and less abrasion, and are therefore characterised by morphologies more similar to primary ash. A final observation is that the distribution of shape descriptors is more disperse for remobilised particles of R150 samples than for primary ash. In the context of the persistent explosive activity at Sabancaya, this possibly reflects the fact that, at a given time, the population of remobilised particles have a varied history, with some particles having undergone aeolian transport for years being more abraded and circular, with other, more recently-erupted particles being more angular.

6. Conclusions

The post-2016 activity of Sabancaya volcano is characterised by frequent Vulcanian explosions, similar to the 2003 activity of Santiaguito (Guatemala) and the 2011–2012 activity of Sakurajima-Showa (Japan). This activity results in a tephra deposit that we identified in the field as being characterised by two main tephra layers, which have a cumulative DRE volume of 0.02 ± 0.01 km^3 (average of $1.1 \pm 0.5 \times 10^{-3}$ km^3 per month DRE from November 2016 to August 2018). In addition, an average DRE volume of $2.3 \pm 1.1 \times 10^{-5}$ km^3 per month is calculated between April 2018 and November 2019 based on tephra collectors, suggesting that the tephra production rate has decreased since 2018, in agreement with the results of Coppola et al. (2022). At Sabancaya, tephra deposits are susceptible to aeolian remobilisation, resulting in potentially intense wind erosion phenomena such as ash storms that can strongly affect the preservation of tephra deposits and, therefore, have an impact on the stratigraphic record. Hence, in such volcanic environments, the erupted volumes are better constrained through multiple complementary sampling strategies, including tephra collection in dedicated containers, especially for low erupted volumes.

We have used an effective sampling method of remobilised particles that involved the separate collection of particles on adhesive paper oriented horizontally at the ground level and oriented vertically above 1.5 m. Results indicate that particles sampled at the ground level are associated with sizes compatible with transport by saltation that minimise the threshold friction velocity, whilst particles sampled above 1.5 m have sizes more consistent with transport by suspension. This sampling strategy can, therefore, be deployed to characterise saltating and suspending particles separately. Small but significant differences are found between the morphologies of primary and remobilised particles, suggesting that particles undergoing transport by saltation are slightly more rounded, even though primary production of tephra and aeolian remobilisation occur simultaneously. Overall, due to favourable meteorological and surface conditions, our work indicates that Sabancaya is an excellent natural laboratory for the study of syn-eruptive aeolian remobilisation processes.

Supplementary data to this article can be found online at https://doi.org/10.1016/j.jvolgeores.2023.107876.

Author contributions

All authors participated in the preparation and realisation of the field campaign. CB, MP, LD and AF studied tephra deposits. NML, RAC, DVH sampled tephra in collectors and provided geophysical data for the analysis of the pulsatory activity of Sabancaya that was conducted by LD. ER and SP acquired high-speed videos and AF acquired high-resolution videos. Sampling of remobilised particles on adhesive paper was conducted by LD, PAJ, AF, ER and SP. LD and PAJ performed PM_{10} measurements with the instrument provided by CH. Particle characterisation and microprobe analysis were performed by AF and LD. AF and LD drafted the manuscript that was reviewed by all authors.

Declaration of Competing Interest

The authors declare that they have no known competing financial interests or personal relationships that could have appeared to influence the work reported in this paper.

Data availability

Data will be made available on request.

Acknowledgements

OVI staff are thanked for their collaboration and their valuable contribution to this study. We are also thankful to Jean-Marie Boccard for preparing samples for microprobe analysis and to Oliver Higgins for supervising microprobe measurements conducted at the University of Geneva. Ali Aluç is thanked for the instructions provided for microscope analysis. We thank Tobias Dürig and an anonymous reviewer for insightful reviews. The study has been funded by the Swiss National Science Foundation (grants no. 200021_169463 and 200021_163152).

Appendix A. Calculation of the threshold friction velocity u_{*t} and determination of the preferential transport mechanism during remobilisation

The balance between aerodynamic forces driving aeolian remobilisation and resisting gravitational and cohesive forces is typically quantified through the threshold friction velocity u_{*t} which is determined from the model of Shao and Lu (2000) as

$$u_{*t} = \sqrt{A_N\left(\frac{\rho_p g d}{\rho_a} + \frac{\gamma}{\rho_a d}\right)}, \tag{A1}$$

with $A_N = 0.0123$ the dimensionless threshold friction velocity for terrestrial surface conditions, $\gamma = 3 \times 10^{-4}$ kg s^{-2} an experimental parameter accounting for the effect of inter-particle cohesion, $g = 9.81$ m s^{-1} the gravitational acceleration on Earth, ρ_p and ρ_a the particle and air density, respectively, and d the particle diameter. For this study, we measure the particle skeletal density (i.e., including non-connected pores) $\rho_p = 2697.4$ kg m^{-3} by Helium pycnometry and we consider that $\rho_a = 0.7$ kg m^{-3}.

In order to determine the preferential transport mechanism of remobilised particles, we define an ideal limit between saltating and suspended grains. This transition occurs at (Scott et al., 1995; Mingari et al., 2020)

$$V_p = \kappa u_*, \tag{A2}$$

where V_p is the particle settling velocity, that depends on the particle size d, $\kappa = 0.4$ is the von Karman constant and u_* is the wind friction velocity. For $V_p > \kappa u_*$, grains are more likely to experience saltation when lifted off the surface. On the contrary, grains are expected to enter in suspension for $V_p < \kappa u_*$. Here, given that only particles with diameters <100 μm (i.e., particle Reynolds number < 0.4 in the atmosphere) enter in suspension for realistic wind friction velocities <2 m s^{-1}, the particle settling velocity is considered to be the Stokes velocity (Mingari et al., 2020)

$$V_p = \frac{g d^2 (\rho_p - \rho_a)}{18 \rho_a \nu}, \tag{A3}$$

with $\nu = 1.5$ m^2 s^{-1}, the kinematic viscosity of air.

Appendix B. Statistical analysis of pulsatory volcanic activity

For stationary time series of pulsatory volcanic activity, the probability of explosion as a function of the repose interval can be well-described by log-logistic models (Dominguez et al., 2016). Log-logistic probability distributions are fitted using the parameters α, that is the median of the repose interval distribution (called 'scale'), and β, that defines the distribution shape. Two parameters are derived from α and β in order to better describe the frequency and variability of time series,

$$\mu = ln(\alpha), \tag{B1}$$

and

$$s = \frac{1}{\beta} \tag{B2}$$

The parameters μ and s are obtained by fitting the probability density function of the repose interval $f(t)$ and the cumulative distribution $F(t)$ by log-logistic distributions

$$f(t) = \frac{exp\left(\frac{ln(t)-\mu}{s}\right)}{s\left[1 + exp\left(\frac{ln(t)-\mu}{s}\right)\right]^2}, \tag{B3}$$

$$F(t) = \frac{1}{1 + exp\left(\frac{ln(t)-\mu}{s}\right)}, \tag{B4}$$

with t the repose interval.

Appendix C. Calculation of tephra volume

The volume of tephra deposits is calculated by fitting the decay of thickness with distance from the vent to three different functions. The first strategy involves fitting the deposit thickness T to an exponential decay law (Pyle, 1989; Fierstein and Nathenson, 1992; Bonadonna and Houghton, 2005)

$$T = T_0 exp\left(-k\sqrt{A}\right), \tag{C1}$$

with T_0 the extrapolated maximum tephra thickness, k the fitted slope of the exponential segment in a semi-log plot and A the area of the isopach contour of thickness T. In this study, given the low quantity of data, we fit our observations with a single exponential segment. The volume V of a single exponential segment can be obtained by integrating (C1) over an infinite area to get

$$V = \frac{2T_0}{k^2} \tag{C2}$$

We also apply power-law and Weibull fitting strategies that have the advantage of better describing the decrease of the mass loading for poorly-exposed deposits. With a power-law fitting, the thickness of tephra deposits decreases with distance from the vent as (Bonadonna and Houghton, 2005)

$$T = T_{pl}\sqrt{A}^{-m}, \tag{C3}$$

where T_{pl} and m are the power-law coefficient and exponent, respectively. Eq. (C3) cannot be integrated between zero and infinity. Hence, proximal and distal integration limits (B and C, respectively) need to be defined in order to obtain an integrated volume of

$$V = \frac{2T_{pl}}{2-m}\left(C^{2-m} - B^{2-m}\right) \tag{C4}$$

Here, we select B based on the extrapolation of the exponential fitting as

$$B = \left(\frac{T_0}{T_{pl}}\right)^{-\frac{1}{m}} \tag{C5}$$

C is determined from the power-law trend, as the value of the square root area for which the tephra thickness equals 0.01 and 0.001 cm (i.e., where the thickness becomes comparable to the diameter of individual fine particles). This results in lower and upper bound estimates for volume which we average.

Finally, the Weibull function describes the decay of the thickness by (Bonadonna and Costa, 2012)

$$T = \theta\left(\frac{\sqrt{A}}{\lambda}\right)^{n-2} exp\left[-\left(\frac{\sqrt{A}}{\lambda}\right)^{n-2}\right], \tag{C6}$$

with θ, λ and n the Weibull fit parameters. This expression is integrated to infinity to obtain the volume

$$V = \frac{2\theta\lambda^2}{n} \tag{C7}$$

For our data, we find $T_0 = 34.6$ cm and $k = 0.2$ km^{-1} using the exponential fitting strategy with a single segment. Using the exponential fitting method, we find a volume of 0.03 ± 0.01 km^3. For the power-law, we find $T_{pl} = 86.8$ cm, $m = 1.2$, $B = 2.2$ km and chose $C = 54$ and 69 km that, respectively, correspond to the square root area at which the power-law thickness equals 0.01 and 0.001 cm. The power-law fitting method gives a volume estimate of 0.06 ± 0.03 km^3. Finally, for the Weibull fitting method, we find $\theta = 14.0$ cm, $\lambda = 12.7$ km and $n = 1.6$. This fitting strategy yields a volume of 0.03 ± 0.02 km^3.

Appendix D. Calculation of tephra masses

For data obtained with tephra collectors, we calculate the mass of tephra accumulated monthly based on the tephra mass load decrease with distance from the vent. The three strategies described in Appendix C are adapted to fit the tephra mass load Y with exponential, power-law and Weibull trends, respectively

$$Y = Y_0 exp\left(-k\sqrt{A}\right), \tag{D1}$$

$$Y = Y_{pl}\sqrt{A}^{-m}, \tag{D2}$$

$$Y = \theta\left(\frac{\sqrt{A}}{\lambda}\right)^{n-2} exp\left[-\left(\frac{\sqrt{A}}{\lambda}\right)^{n-2}\right], \tag{D3}$$

with Y_0 the extrapolated maximum mass load and Y_{pl} the power-law coefficient. The fitting parameters k, m, θ, λ and n are described in Appendix C, and A corresponds to the area of the isomass contour of mass load Y. The mass M of a single exponential segment can be estimated as

$$M = \frac{2Y_0}{k^2} \tag{D4}$$

The mass is estimated from the power-law fitting as

$$M = \frac{2Y_{pl}}{2-m}\left(C^{2-m} - B^{2-m}\right), \tag{D5}$$

where B is estimated by extrapolating the exponential fitting as

$$B = \left(\frac{Y_0}{Y_{pl}}\right)^{-\frac{1}{m}} \tag{D6}$$

Here, we calculate C from the value of the square root area for which the power-law trend equals to 0.005 and 0.0005 kg m^{-2} month^{-1}. Finally, the Weibull function is integrated to obtain the total mass

$$M = \frac{2\theta\lambda^2}{n} \quad \text{(D7)}$$

We find $Y_0 = 1.6 \times 10^6$ kg km^{-2} month^{-1}, $k = 0.2$ km^{-1} and $M = 6.8 \pm 3.5 \times 10^7$ kg per month, using the exponential fitting strategy with a single segment. For the power-law, we find $Y_{pl} = 12.8 \times 10^6$ kg km^{-2} month^{-1} and $m = 1.7$. The integration limits are $B = 2.8$ km and $C = 26$ and 36 km, that respectively correspond to the square root area at which the power-law trend equals to 0.005 and 0.0005 kg m^{-2} month^{-1}. The power-law fitting method gives a mass estimate of $6.1 \pm 2.8 \times 10^7$ kg per month. Finally, for the Weibull fitting method, we find $\theta = 0.5 \times 10^6$ kg km^{-2} month^{-1}, $\lambda = 8.7$ km and $n = 1.0$. This fitting strategy yields a mass estimate of $6.2 \pm 2.7 \times 10^7$ kg per month.

References

Adams, N., de Silva, S., Self, S., Salas, G., Schubring, S., Permenter, J., et al., 2001. The physical volcanology of the 1600 eruption of Huaynaputina, southern Peru. Bull. Volcanol. 62, 493–518. https://doi.org/10.1007/s004450000105.

Aguilar, R., 2019. Exposure-based risk assessment of tephra-fall associated with long-lasting Vulcanian eruptions at Sabancaya volcano, Peru. In: These de Specialisation in the Assessment and Management of Geological and Climate Related Risk - CERG-C 2018. University of Geneva, Geneva.

Aguilar, R., Taipe, E., Antayhua, Y., Ortega, M., Apaza, F., Cruz, L., 2021. Hazard assessment studies and multiparametric volcano monitoring developed by the Instituto Geológico, Minero y Metalúrgico in Peru. Volcanica 4 (S1), 73–82. https://doi.org/10.30909/vol.04.S1.7392.

Alcalá-Reygosa, J., Palaciaos, D., Zamorano, J.J., Vázquez-Selem, L., 2011. Last Glacial Maximum and deglaciaton of Ampato volcanic complex, Southern Peru. Rev. Cuaternario Geomorfol. 25, 121–136.

Arnalds, O., Thorarinsdottir, E.F., Thorsson, J., Waldhauserova, P.D., Agustsdottir, A.M., 2013. An extreme wind erosion event of the fresh Eyjafjallajökull 2010 volcanic ash. Sci. Rep. 3, 1257. https://doi.org/10.1038/srep01257.

Bagheri, G., Rossi, E., Biass, S., Bonadonna, C., 2016. Timing and nature of volcanic particle clusters based on field and numerical investigations. J. Volcanol. Geotherm. Res. 327, 520–530. https://doi.org/10.1016/j.jvolgeores.2016.09.009.

Bagnold, R.A., 1941. The Physics of Blown Sand and Desert Dunes. New York.

Balme, M., Greeley, R., 2006. Dust devils on earth and mars. Rev. Geophys. 44, RG3003. https://doi.org/10.1029/2005RG000188.

Barclay, J., Few, R., Armijos, M.T., Phillips, J.C., Pyle, D.M., Hicks, A., et al., 2019. Livelihoods, wellbeing and the risk to life during volcanic eruptions. Front. Earth Sci. 7, 205. https://doi.org/10.3389/feart.2019.00205.

Bernard, B., 2013. Homemade ashmeter: a low-cost, high-efficiency solution to improve tephra field-data collection for contemporary explosive eruptions. J. Appl. Volcanol. 2, 1. https://doi.org/10.1186/2191-5040-2-1.

Biass, S., Bagheri, G., Aeberhard, W., Bonadonna, C., 2013. TError: towards a better quantification of the uncertainty propagated during the characterization of tephra deposits. Stat. Volcanol. 1, 1–27. https://doi.org/10.5038/2163-338X.1.2.

Biass, S., Bonadonna, C., Connor, L., Connor, C., 2016. TephraProb: a Matlab package for probabilistic hazard assessments of tephra fallout. J. Appl. Volcanol. 5, 10. https://doi.org/10.1186/s13617-016-0050-5.

Biass, S., Bonadonna, C., Houghton, B.F., 2019. A step-by-step evaluation of empirical methods to quantify eruption source parameters from tephra-fall deposits. J. Appl. Volcanol. 8, 1. https://doi.org/10.1186/s13617-018-0081-1.

Blong, R., Enright, N., Grasso, P., 2017. Preservation of thin tephra. J. Appl. Volcanol. 6, 10. https://doi.org/10.1186/s13617-017-0059-4.

Bonadonna, C., Costa, A., 2012. Estimating the volume of tephra deposits: a new simple strategy. Geology 40, 415–418. https://doi.org/10.1130/G32769.1.

Bonadonna, C., Costa, A., 2013. Plume height, volume, and classification of explosive volcanic eruptions based on the Weibull function. Bull. Volcanol. 75 https://doi.org/10.1007/s00445-013-0742-1.

Bonadonna, C., Houghton, B.F., 2002. Total grain-size distribution and volume of tephra-fall deposits. Bull. Volcanol. 67, 441–456. https://doi.org/10.1007/s00445-004-0386-2.

Bonadonna, C., Macedonio, G., Sparks, R.S.J., 2005. Numerical modelling of tephra fallout associated with dome collapses and Vulcanian explosions: application to hazard assessment on Montserrat. Geol. Soc. Lond. Mem. 21, 517–537. https://doi.org/10.1144/GSL.MEM.2002.021.01.23.

Bonadonna, C., Genco, R., Gouhier, M., Pistolesi, M., Cioni, R., Alfano, F., et al., 2011. Tephra sedimentation during the 2010 Eyjafjallajökull eruption (Iceland) from deposit, radar, and satellite observations. J. Geophys. Res. 116 https://doi.org/10.1029/2011JB008462.

Bonadonna, C., Biass, S., Costa, A., 2015. Physical characterization of explosive volcanic eruptions based on tephra deposits: Propagation of uncertainties and sensitivity analysis. J. Volcanol. Geotherm. Res. 296, 80–100. https://doi.org/10.1016/j.jvolgeores.2015.03.009.

Bonadonna, C., Cioni, R., Costa, A., Druitt, T., Phillips, J., Pioli, L., et al., 2016. MeMoVolc report on classification and dynamics of volcanic explosive eruptions. Bull. Volcanol. 78, 84. https://doi.org/10.1007/s00445-016-1071-y.

Bonadonna, C., Pistolesi, M., Dominguez, L., Freret-Lorgeril, V., Rossi, E., Fries, A., et al., 2023. Tephra sedimentation and grainsize associated with pulsatory activity: the 2021 Tajogaite eruption of Cumbre Vieja (La Palma, Canary Islands, Spain). Front. Earth Sci. 11, 1166073. https://doi.org/10.3389/feart.2023.1166073.

Brown, R.J., Bonadonna, C., Durant, A.J., 2012. A review of volcanic ash aggregation. Phys. Chem. Earth Parts ABC 45–46, 65–78. https://doi.org/10.1016/j.pce.2011.11.001.

Bulmer, M., Johnston, A., Engle, F., 1999. Analysis of sabancaya Volcano, Southern Peru, Using Radarsat and Lansat TM Data. Appl. Dev. Res. Oppor. ADRO.

Chojnicki, K.N., Clarke, A.B., Phillips, J.C., Adrian, R.J., 2015. Rise dynamics of unsteady laboratory jets with implications for volcanic plumes. Earth Planet. Sci. Lett. 412, 186–196. https://doi.org/10.1016/j.epsl.2014.11.046.

Clarke, A.B., Esposti Ongaro, T., Belousov, A., 2015. Vulcanian eruptions. In: The Encyclopedia of Volcanoes. Elsevier, pp. 505–518. https://doi.org/10.1016/B978-0-12-385938-9.00028-6.

Cobeñas, G., Thouret, J.-C., Bonadonna, C., Boivin, P., 2012. The c.2030yr BP Plinian eruption of El Misti volcano, Peru: eruption dynamics and hazard implications. J. Volcanol. Geotherm. Res. 241–242, 105–120. https://doi.org/10.1016/j.jvolgeores.2012.06.006.

Cole, P.D., Fernandez, E., Duarte, E., Duncan, A.M., 2005. Explosive activity and generation mechanisms of pyroclastic flows at Arenal volcano, Costa Rica between 1987 and 2001. Bull. Volcanol. 67, 695–716. https://doi.org/10.1007/s00445-004-0402-6.

Constantinescu, R., White, J.T., Connor, C.B., Hopulele-Gligor, A., Charbonnier, S., Thouret, J.-C., et al., 2022. Uncertainty quantification of eruption source parameters estimated from tephra fall deposits. Geophys. Res. Lett. 49 https://doi.org/10.1029/2021GL097425.

Coppola, D., Valade, S., Masias, P., Laiolo, M., Massimetti, F., Campus, A., et al., 2022. Shallow magma convection evidenced by excess degassing and thermal radiation during the dome-forming Sabancaya eruption (2012−2020). Bull. Volcanol. 84, 16. https://doi.org/10.1007/s00445-022-01523-1.

Costa, A, Caricchi, L, Bagdassarov, N, 2009. A model for the rheology of particle-bearing suspensions and partially molten rocks. Geochem. Geophys. Geosyst. 10, Q03010. https://doi.org/10.1029/2008GC002138.

Cutler, N.A., Streeter, R.T., Marple, J., Shotter, L.R., Yeoh, J.S., Dugmore, A.J., 2018. Tephra transformations: variable preservation of tephra layers from two well-studied eruptions. Bull. Volcanol. 80, 77. https://doi.org/10.1007/s00445-018-1251-z.

Del Bello, E., Taddeucci, J., Merriso, J.P., Rasmussen, K.R., Andronico, D., Ricci, T., Scarlato, P., Iversen, J.J., 2021. Field-based measurements of volcanic ash resuspension by wind. Earth Planet. Sci. Lett. 554, 116684. https://doi.org/10.1016/j.epsl.2020.116684.

Del Bello, E., Taddeucci, J., Merrison, J.P., Alois, S., Iversen, J.J., Scarlato, P., 2018. Experimental simulations of volcanic ash resuspension by wind under the effects of atmospheric humidity. Sci. Rep. 8, 14509. https://doi.org/10.1038/s41598-018-32807-2.

Del Carpio Calienes, J.A., Rivera, M., Puma, N., Cruz, J., Torres, J.L., Vargas, K., et al., 2020. Evaluación geofísica del comportamiento dinámico actual del volcán Sabancaya, periodo 1 de diciembre de 2019-2 de febrero de 2020. Available at. http://hdl.handle.net/20.500.12816/4753.

Dellino, P., La Volpe, L., 1996. Image processing analysis in reconstructing fragmentation and transportation mechanisms of pyroclastic deposits. The case of Monte Pilato-Rocche Rosse eruptions, Lipari (Aeolian islands, Italy). J. Volcanol. Geotherm. Res. 71, 13–29. https://doi.org/10.1016/0377-0273(95)00062-3.

Dominguez, L., Pioli, L., Bonadonna, C., Connor, C.B., Andronico, D., Harris, A.J.L., et al., 2016. Quantifying unsteadiness and dynamics of pulsatory volcanic activity. Earth Planet. Sci. Lett. 444, 160–168. https://doi.org/10.1016/j.epsl.2016.03.048.

Dominguez, L., Rossi, E., Mingari, L., Bonadonna, C., Forte, P., Panebianco, J.E., et al., 2020a. Mass flux decay timescales of volcanic particles due to aeolian processes in the Argentinian Patagonia steppe. Sci. Rep. 10, 14456. https://doi.org/10.1038/s41598-020-71022-w.

Dominguez, L., Bonadonna, C., Forte, P., Jarvis, P.A., Cioni, R., Mingari, L., et al., 2020b. Aeolian remobilisation of the 2011-Cordón Caulle tephra-fallout deposit: example of an important process in the life cycle of volcanic ash. Front. Earth Sci. 7, 343. https://doi.org/10.3389/feart.2019.00343.

Druitt, T.H., Young, S.R., Baptie, B., Bonadonna, C., Calder, E.S., Clarke, A.B., et al., 2002. Episodes of cyclic Vulcanian explosive activity yith fountain collapse at Soufrière Hills Volcano, Montserrat. In: Druitt, T.H., Kokelaar, B.P. (Eds.), The eruption of Soufrière Hills Volcano, Montserrat, from 1995 to 1999, Memoirs. Geological Society, London, pp. 281–306.

Dugmore, A., Streeter, R., Cutler, N., 2018. The role of vegetation cover and slope angle in tephra layer preservation and implications for Quaternary tephrostratigraphy. Palaeogeogr. Palaeoclimatol. Palaeoecol. 489, 105–116. https://doi.org/10.1016/j.palaeo.2017.10.002.

Dugmore, A.J., Thompson, P.I.J., Streeter, R.T., Cutler, N.A., Newton, A.J., Kirkbride, M.P., 2020. The interpretative value of transformed tephra sequences. J. Quat. Sci. 35, 23–38. https://doi.org/10.1002/jqs.3174.

Dürig, T., Gudmundsson, M.T., Karmann, S., Zimanowski, B., Dellino, P., Rietze, M., et al., 2015. Mass eruption rates in pulsating eruptions estimated from video analysis of the gas thrust-buoyancy transition—a case study of the 2010 eruption of

Eyjafjallajökull, Iceland. Earth Planets Space 67, 180. https://doi.org/10.1186/s40623-015-0351-7.
Dürig, T., Bowman, M., White, J., Murch, A., Mele, D., Verolino, A., et al., 2018. PARTIcle Shape ANalyzer PARTISAN – an open source tool for multi-standard two-dimensional particle morphometry analysis. Ann. Geophys. 61, 3. https://doi.org/10.4401/ag-7865.
Dürig, T., Schmidt, L.S., White, J.D.L., Bowman, M.H., 2020. DendroScan: an open source tool to conduct comparative statistical tests and dendrogrammatic analyses on particle morphometry. Sci. Rep. 10, 21682. https://doi.org/10.1038/s41598-020-78698-0.
Dürig, T., Ross, P.-S., Dellino, P., White, J.D.L., Mele, D., Comida, P.P., 2021. A review of statistical tools for morphometric analysis of juvenile pyroclasts. Bull. Volcanol. 83, 79. https://doi.org/10.1007/s00445-021-01500-0.
Elissondo, M., Baumann, V., Bonadonna, C., Pistolesi, M., Cioni, R., Bertagnini, A., et al., 2016. Chronology and impact of the 2011 Cordón Caulle eruption, Chile. Nat. Hazards Earth Syst. Sci. 16, 675–704. https://doi.org/10.5194/nhess-16-675-2016.
Engwell, S., Sparks, R., Aspinall, W., 2013. Quantifying uncertainties in the measurement of tephra fall thickness. J. Appl. Volcanol. 2, 5. https://doi.org/10.1186/2191-5040-2-5.
Etyemezian, V., Gillies, J.A., Mastin, L.G., Crawford, A., Hasson, R., Van Eaton, A.R., et al., 2019. Laboratory experiments of volcanic ash resuspension by wind. J. Geophys. Res.-Atmos. 124, 9534–9560. https://doi.org/10.1029/2018JD030076.
Eychenne, J., Le Pennec, J.-L., Ramón, P., Yepes, H., 2013. Dynamics of explosive paroxysms at open-vent andesitic systems: High-resolution mass distribution analyses of the 2006 Tungurahua fall deposit (Ecuador). Earth Planet. Sci. Lett. 361, 343–355. https://doi.org/10.1016/j.epsl.2012.11.002.
Fierstein, J., Nathenson, M., 1992. Another look at the calculation of fallout tephra volumes. Bull. Volcanol. 54, 156–167. https://doi.org/10.1007/BF00278005.
Folch, A., Mingari, L., Osores, M.S., Collini, E., 2014. Modeling volcanic ash resuspension – application to the 14–18 October 2011 outbreak episode in central Patagonia, Argentina. Nat. Hazards Earth Syst. Sci. 14, 119–133. https://doi.org/10.5194/nhess-14-119-2014.
Fontijn, K., Lachowycz, S.M., Rawson, H., Pyle, D.M., Mather, T.A., Naranjo, J.A., et al., 2014. Late Quaternary tephrostratigraphy of southern Chile and Argentina. Quat. Sci. Rev. 89, 70–84. https://doi.org/10.1016/j.quascirev.2014.02.007.
Forte, P., Domínguez, L., Bonadonna, C., Gregg, C.E., Bran, D., Bird, D., et al., 2018. Ash resuspension related to the 2011–2012 Cordón Caulle eruption, Chile, in a rural community of Patagonia, Argentina. J. Volcanol. Geotherm. Res. 350, 18–32. https://doi.org/10.1016/j.jvolgeores.2017.11.021.
Freret-Lorgeril, V., Donnadieu, F., Eychenne, J., Soriaux, C., Latchimy, T., 2019. In situ terminal settling velocity measurements at Stromboli volcano: Input from physical characterization of ash. J. Volcanol. Geotherm. Res. 374, 62–79. https://doi.org/10.1016/j.jvolgeores.2019.02.005.
Gerbe, M.-C., Thouret, J.-C., 2004. Role of magma mixing in the petrogenesis of tephra erupted during the 1990–98 explosive activity of Nevado Sabancaya, southern Peru. Bull. Volcanol. 66, 541–561. https://doi.org/10.1007/s00445-004-0340-3.
Giordano, D., Russell, J.K., Dingwell, D.B., 2008. Viscosity of magmatic liquids: A model. Earth Planet. Sci. Lett. 271, 123–134.
Gonnermann, H.M., Manga, M., 2012. Dynamics of magma ascent in the volcanic conduit: modeling volcanic processes. The Physics and Mathematics of Volcanism. Cambridge University Press, pp. 55–84. https://doi.org/10.2138/am.2014.648.
Hammond, K., Beckett, F., 2019. Forecasting resuspended ash clouds in Iceland at the London VAAC. Weather 74, 167–171. https://doi.org/10.1002/wea.3398.
Hersbach, H., Bell, B., Berrisford, P., Hirahara, S., Horányi, A., Muñoz-Sabater, J., et al., 2020. The ERA5 global reanalysis. Q. J. R. Meteorol. Soc. 146, 1999–2049. https://doi.org/10.1002/qj.3803.
Houghton, B., Carey, R.J., 2015. Pyroclastic fall deposits. In: The Encyclopedia of Volcanoes. Elsevier, pp. 599–616. https://doi.org/10.1016/B978-0-12-385938-9.00034-1.
Inman, D.L., 1952. Measures for describing the size distribution of sediments. SEPM J. Sediment. Res. 22 https://doi.org/10.1306/D42694DB-2B26-11D7-8648000102C1865D.
Jarvis, P.A., Bonadonna, C., Dominguez, L., Forte, P., Frischknecht, C., Bran, D., et al., 2020. Aeolian remobilisation of volcanic ash: outcomes of a workshop in the argentinian patagonia. Front. Earth Sci. 8 https://doi.org/10.3389/feart.2020.575184.
Jay, J.A., Delgado, F.J., Torres, J.L., Pritchard, M.E., Macedo, O., Aguilar, V., 2015. Deformation and seismicity near Sabancaya volcano, southern Peru, from 2002 to 2015: Deformation and seismicity at Sabancaya. Geophys. Res. Lett. 42, 2780–2788. https://doi.org/10.1002/2015GL063589.
Juvigné, E., Thouret, J.Cl., Gilot, E., Leclercq, L., Gourgaud, A., 1998. L'activité du volcan Nevado Sabancaya (Pérou) au cours de l'Holocène [activity of Nevado Sabancaya volcano (Peru) throughout the Holocene]. Quaternaire 9, 45–51. https://doi.org/10.3406/quate.1998.2105.
Juvigné, E., Thouret, J., Loutsch, I., Lamadon, S., Frechen, M., Fontugne, M., et al., 2008. Retombées volcaniques dans des tourbières et lacs autour du massif des Nevados Ampato et Sabancaya (Pérou méridional, Andes Centrales). Quaternaire 157–173. https://doi.org/10.4000/quaternaire.3362.
Klawonn, M., Houghton, B.F., Swanson, D.A., Fagents, S.A., Wessel, P., Wolfe, C.J., 2014a. Constraining explosive volcanism: subjective choices during estimates of eruption magnitude. Bull. Volcanol. 76, 793. https://doi.org/10.1007/s00445-013-0793-3.
Klawonn, M., Houghton, B.F., Swanson, D.A., Fagents, S.A., Wessel, P., Wolfe, C.J., 2014b. From field data to volumes: constraining uncertainties in pyroclastic eruption parameters. Bull. Volcanol. 76, 839. https://doi.org/10.1007/s00445-014-0839-1.
Kok, J.F., Parteli, E.J.R., Michaels, T.I., Karam, D.B., 2012. The physics of wind-blown sand and dust. Rep. Prog. Phys. 75, 106901 https://doi.org/10.1088/0034-4885/75/10/106901.
Liu, E.J., Cashman, K.V., Beckett, F.M., Witham, C.S., Leadbetter, S.J., Hort, M.C., et al., 2014. Ash mists and brown snow: Remobilization of volcanic ASH from recent Icelandic eruptions: ash mists and brown snow. J. Geophys. Res.-Atmos. 119, 9463–9480. https://doi.org/10.1002/2014JD021598.
Liu, E.J., Cashman, K.V., Rust, A.C., 2015. Optimising shape analysis to quantify volcanic ash morphology. GeoResJ 8, 14–30. https://doi.org/10.1016/j.grj.2015.09.001.
Machacca, R., Del Carpio, J., Rivera, M., Tavera, H., Macedo, L., Concha, J.A., et al., 2021. Monitoring of active volcanoes in Peru by the Instituto Geofísico del Perú. Volcanica 4, 49–71. https://doi.org/10.30909/vol.04.S1.4971.
Machacca, R., Lesage, P., Tavera, H., Pesicek, J.D., Caudron, C., Torres, J.L., et al., 2023. The 2013–2020 seismic activity at Sabancaya Volcano (Peru): Long lasting unrest and eruption. J. Volcanol. Geotherm. Res. 435, 107767 https://doi.org/10.1016/j.jvolgeores.2023.107767.
MacQueen, P., Delgado, F., Reath, K., Pritchard, M.E., Bagnardi, M., Milillo, P., et al., 2020. Volcano-tectonic interactions at Sabancaya Volcano, Peru: eruptions, magmatic inflation, moderate earthquakes, and fault creep. J. Geophys. Res. Solid Earth 125. https://doi.org/10.1029/2019JB019281.
Manrique, N., Lazarte, I., Cueva, K., Rivera, M., Aguilar, R., 2018a. Actividad del volcán Sabancaya (Perú) 2016–2017: Características de las emisiones de ceniza y análisis granulométrico.
Manrique, N., Lazarte, I., Rivera, M., Cueva, K., Japura, S., Aguilar, R., 2018b. Actividad del volcán Sabancaya (Perú) 2016–2017: observaciones petrográficas y geoquímicas de los depósitos de tefras del 2017. In: Hazard and risk mapping (The Arequipa-El Misti case study and other threatened cities).
Mele, D., Dellino, P., Sulpizio, R., Braia, G., 2011. A systematic investigation on the aerodynamics of ash particles. J. Volcanol. Geotherm. Res. 203, 1–11. https://doi.org/10.1016/j.jvolgeores.2011.04.004.
Mingari, L., Folch, A., Dominguez, L., Bonadonna, C., 2020. Volcanic Ash Resuspension in Patagonia: Numerical Simulations and Observations. Atmosphere 11, 977. https://doi.org/10.3390/atmos11090977.
Naismith, A.K., Matthew Watson, I., Escobar-Wolf, R., Chigna, G., Thomas, H., Coppola, D., et al., 2019. Eruption frequency patterns through time for the current (1999–2018) activity cycle at Volcán de Fuego derived from remote sensing data: evidence for an accelerating cycle of explosive paroxysms and potential implications of eruptive activity. J. Volcanol. Geotherm. Res. 371, 206–219. https://doi.org/10.1016/j.jvolgeores.2019.01.001.
Oishi, M., Nishiki, K., Geshi, N., Furukawa, R., Ishizuka, Y., Oikawa, T., et al., 2018. Distribution and mass of tephra-fall deposits from volcanic eruptions of Sakurajima Volcano based on posteruption surveys. Bull. Volcanol. 80, 42. https://doi.org/10.1007/s00445-018-1215-3.
Panebianco, J.E., Mendez, M.J., Buschiazzo, D.E., Bran, D., Gaitán, J.J., 2017. Dynamics of volcanic ash remobilisation by wind through the Patagonian steppe after the eruption of Cordón Caulle, 2011. Sci. Rep. 7, 45529. https://doi.org/10.1038/srep45529.
Pistolesi, M., Aravena, A., Costantini, L., Vigiani, C., Cioni, R., Bonadonna, C., 2021. Explosive behavior of intermediate magmas: The example of Cotopaxi volcano (Ecuador). Geochem. Geophys. Geosys. 22, e2021GC009991 https://doi.org/10.1029/2021GC009991.
Pistolesi, M., Cioni, R., Bonadonna, C., Elissondo, M., Baumann, V., Bertagnini, A., et al., 2015. Complex dynamics of small-moderate volcanic events: the example of the 2011 rhyolitic Cordón Caulle eruption, Chile. Bull. Volcanol. 77 https://doi.org/10.1007/s00445-014-0898-3.
Poulidis, A.P., Takemi, T., Iguchi, M., Disaster Prevention Research Institute (DPRI), Kyoto University Gokasho, Uji, Kyoto 611-0011, Japan, Sakurajima Volcano Research Center, Disaster Prevention Research Institute (DPRI), Kyoto University, Kagoshima, Japan, 2019. Experimental high-resolution forecasting of volcanic ash hazard at Sakurajima, Japan. J. Disaster Res. 14, 786–797. https://doi.org/10.20965/jdr.2019.p0786.
Prival, J.-M., Thouret, J.-C., Japura, S., Gurioli, L., Bonadonna, C., Mariño, J., et al., 2020. New insights into eruption source parameters of the 1600 CE Huaynaputina Plinian eruption, Peru. Bull. Volcanol. 82, 7. https://doi.org/10.1007/s00445-019-1340-7.
Pye, K., 1987. Aeolian dust and dust deposits. Academic Press, London ; Orlando.
Pyle, D.M., 1989. The thickness, volume and grainsize of tephra fall deposits. Bull. Volcanol. 51, 1–15. https://doi.org/10.1007/BF01086757.
Ripepe, M., Bonadonna, C., Folch, A., Delle Donne, D., Lacanna, G., Marchetti, E., et al., 2013. Ash-plume dynamics and eruption source parameters by infrasound and thermal imagery: the 2010 Eyjafjallajökull eruption. Earth Planet. Sci. Lett. 366, 112–121. https://doi.org/10.1016/j.epsl.2013.02.005.
Rivera, M., Thouret, J.-C., Samaniego, P., Le Pennec, J.-L., 2014. The 2006–2009 activity of the Ubinas volcano (Peru): Petrology of the 2006 eruptive products and insights into genesis of andesite magmas, magma recharge and plumbing system. J. Volcanol. Geotherm. Res. 270, 122–141. https://doi.org/10.1016/j.jvolgeores.2013.11.010.
Ross, P.-S., Dürig, T., Comida, P.P., Lefebvre, N., White, J.D.L., Andronico, D., et al., 2022. Standardized analysis of juvenile pyroclasts in comparative studies of primary magma fragmentation; 1. Overview and workflow. Bull. Volcanol. 84, 13. https://doi.org/10.1007/s00445-021-01516-6.
Samaniego, P., Rivera, M., Mariño, J., Guillou, H., Liorzou, C., Zerathe, S., et al., 2016. The eruptive chronology of the Ampato–Sabancaya volcanic complex (Southern Peru). J. Volcanol. Geotherm. Res. 323, 110–128. https://doi.org/10.1016/j.jvolgeores.2016.04.038.

Schmith, J., Höskuldsson, Á., Holm, P.M., 2017. Grain shape of basaltic ash populations: implications for fragmentation. Bull. Volcanol. 79, 14. https://doi.org/10.1007/s00445-016-1093-5.

Scott, W.D., Hopwood, J.M., Summers, K.J., 1995. A mathematical model of suspension with saltation. Acta Mech. 108, 1–22. https://doi.org/10.1007/BF01177324.

Scott, J.A.J., Mather, T.A., Pyle, D.M., Rose, W.I., Chigna, G., 2012. The magmatic plumbing system beneath Santiaguito Volcano, Guatemala. J. Volcanol. Geotherm. Res. 237–238, 54–68. https://doi.org/10.1016/j.jvolgeores.2012.05.014.

Selby, M.J., 1982. Hillslope Materials and Processes. Oxford University Press, Oxford [Oxfordshire] ; New York.

Shao, Y., Lu, H., 2000. A simple expression for wind erosion threshold friction velocity. J. Geophys. Res.-Atmos. 105, 22437–22443. https://doi.org/10.1029/2000JD900304.

Shao, Y., Raupach, M.R., Findlater, P.A., 1993. Effect of saltation bombardment on the entrainment of dust by wind. J. Geophys. Res. 98, 12719. https://doi.org/10.1029/93JD00396.

Siebert, L., Simkin, T., Kimberly, P., 2010. Volcanoes of the World, 3rd ed. University of California Press: Smithsonian Institution, Washington, D.C. : Berkeley.

Simionato, R., Jarvis, P.A., Rossi, E., Bonadonna, C., 2022. PlumeTraP: a new MATLAB-based algorithm to detect and parametrize volcanic plumes from visible-wavelength images. Remote Sens. 14, 1766. https://doi.org/10.3390/rs14071766.

Sinclair, P.C., 1969. General characteristics of dust devils. J. Appl. Meteorol. Climatol. 8, 32–45. https://doi.org/10.1175/1520-0450(1969)008<0032:GCODD>2.0.CO;2.

Taddeucci, J., Edmonds, M., Houghton, B., James, M.R., Vergniolle, S., 2015. Hawaiian and strombolian eruptions. In: The Encyclopedia of Volcanoes. Elsevier, pp. 485–503. https://doi.org/10.1016/B978-0-12-385938-9.00027-4.

Thouret, J.C., Guillande, R., Huaman, D., Gourgaud, A., Salas, G., Chorowicz, J., 1994. L'Activite actuelle du Nevado Sabancaya (sud Perou); reconnaissance geologique et satellitaire, evaluation et cartographie des menaces volcaniques. Bull. Société Géologique Fr. 165, 49–63.

Thouret, J.-C., Juvigné, E., Gourgaud, A., Boivin, P., Dávila, J., 2002. Reconstruction of the AD 1600 Huaynaputina eruption based on the correlation of geologic evidence with early Spanish chronicles 1 1Data Repository at http://www.elsevier.com/locate/jvolgeores see 'Electronic Supplements'. J. Volcanol. Geotherm. Res. 115, 529–570. https://doi.org/10.1016/S0377-0273(01)00323-7.

Valdivia, D., 2019. Muestreo de cenizas en los alrededores del volcán Sabancaya. Available at: https://repositorio.ingemmet.gob.pe/bitstream/20.500.12544/2489/1/A6954-Muestreo_de_cenizas_volcán_Sabancaya.pdf.

Valentine, G.A., Gregg, T.K.P., 2008. Continental basaltic volcanoes — Processes and problems. J. Volcanol. Geotherm. Res. 177, 857–873. https://doi.org/10.1016/j.jvolgeores.2008.01.050.

Varley, N., Johnson, J., Ruiz, M., Reyes, G., Martin, K., 2006. Applying statistical analysis to understanding the dynamics of volcanic explosions. Stat. Volcanol. 1, 57.

Varley, N., Arámbula-Mendoza, R., Reyes-Dávila, G., Sanderson, R., Stevenson, J., 2010. Generation of Vulcanian activity and long-period seismicity at Volcán de Colima, Mexico. J. Volcanol. Geotherm. Res. 198, 45–56. https://doi.org/10.1016/j.jvolgeores.2010.08.009.

Wilson, T.M., Cole, J.W., Stewart, C., Cronin, S.J., Johnston, D.M., 2011. Ash storms: impacts of wind-remobilised volcanic ash on rural communities and agriculture following the 1991 Hudson eruption, southern Patagonia, Chile. Bull. Volcanol. 73, 223–239. https://doi.org/10.1007/s00445-010-0396-1.

World Health Organization, 2021. WHO global air quality guidelines: particulate matter (PM2.5 and PM10), ozone, nitrogen dioxide, sulfur dioxide and carbon monoxide. World Health Organization, Geneva. Available at: https://apps.who.int/iris/handle/10665/345329 [Accessed September 27, 2022].